Niels Bohr Institute

Measurements of flow vector fluctuations in p–Pb collisions at $\sqrt{s_{\mathrm{NN}}} = 5.02$ TeV with ALICE

Mathias Labonte

A Thesis submitted in partial fulfillment of the requirements for the degree of Master of Science

Copenhagen, Denmark
May 2022

Acknowledgements

When I first learned about the research being done with ALICE at NBI, I knew I had to be a part of it. During our first meeting, seeing the passion for physics of my then-future supervisor, You, made me excited for a year that would turn out to teach me a lot about science and many other things. I need to thank You for the great year, the many opportunities he helped me pursue, and the lessons I learned under his tutelage. I hope to apply these lessons in the future as I begin my doctoral studies in California. I will try my best to represent the group and NBI well.

Another critical thank you goes to my co-supervisor Zuzana, who (with supreme patience) aided me in countless technical, professional, and personal matters, and was instrumental in helping me reach the finish line. I hope my baking and snacks throughout the year was sufficient repayment. Thank you for your friendship. I will deeply miss our lunch breaks and after-work beers.

A sincere thank you goes to Emil. Thank you for your friendship, lunch-time talks, and faithful train operation. Thank you to Christian Holm for the suggestions on my thesis and sharing your technical knowledge.

I would like to acknowledge my friends and fellow master's students Jonathan and Arnau, who made coming to the office fun, and consumed inordinate amounts of coffee with me. Thank you Mitch for your long-time friendship; you were my long-distance master's buddy. Thanks to Espen for the fun times and letting me watch you play video games. Thank you Emma for your encouragement and motivation, which made the last part of my degree so much better.

Most importantly, I want to thank my parents for their unconditional love, support, and guidance. You have played a huge part in what I have accomplished so far. Thank you for teaching me the values that made me capable of completing this thesis.

Abstract

The Quark Gluon Plasma (QGP), a state of hot and dense matter thought to be present one millionth of a second after the big bang, is believed to be created in ultra-relativistic heavy ion collisions at the large hadron collider (LHC). Experimental study of heavy ion collisions provide constraints on the initial conditions and dynamic properties of the created medium. Recent measurements in small system collisions, including proton-lead (p–Pb), have yielded a number of surprising results that are comparable to measurements large systems, suggesting that small and large collision systems could produce similar matter and requires theoretical understanding. Measurements of anisotropic flow in particular have generated intrigue regarding these similairites. An understanding of the origin of a flow signal in p–Pb collisions is required and the subject of intense study.

One method of probing the origin of a flow signal in p–Pb collisions is through the study of p_{T} dependent flow vector fluctuations, a phenomenon which can be modelled hydrodynamically in lead–lead (Pb–Pb) collisions. Similar measurements of flow vector fluctuations in p–Pb can be used to investigate the origin of a flow signal in small systems through comparison to theoretical modelling. This thesis measures flow vector fluctuations in p–Pb systems at $\sqrt{s_{\mathrm{NN}}}$= 5.02 TeV using state of the art non-flow subtraction techniques and high sample size run-2 ALICE data. These measurements provide important constraints on future theoretical models, which will in turn constrain speculation over the source of a flow signal in small systems.

Table of Contents

Figures

Tables

Chapter 1

Introduction

In this chapter, an overview of the field of particle physics is briefly elucidated, with an emphasis on the strong force. The quark gluon plasma and the field of heavy ion physics is then introduced. Lastly, a motivation for the analysis performed in this work is presented.

1.1 The Standard Model

Nature's most basic objects are, point like objects known as *particles*. The most successful theoretical description of fundamental particles observed in nature is known as the *Standard Model* (SM), whose rules are governed by a mathematical framework known as *quantum field theory*. The Standard Model is successful in describing three out of the four fundamental forces of nature, namely the electromagnetic force, and the strong and weak nuclear forces. A quantum theory of gravity, however, has yet to show compatibility with the other forces of nature within the confines of the Standard Model. It is for this reason, among others, that the Standard Model is said to be an incomplete theory.

The Standard Model describes two main classes of fundamental particles; bosons and fermions who follow different statistical laws, namely Fermi–Dirac statistics (fermions) and Bose-Einstien statistics (bosons). Spin–1 vector bosons are known as the "force carriers" of the Standard Model. In other words, they are responsible for transmitting a force from one interacting particle to another. The electromagnetic force is mediated by photons, the weak nuclear force interacts via W and Z bosons, and the strong interaction is 'carried' by

gluons. The final boson described by the Standard Model is the Higgs boson– a spin 0 scalar particle, whereby interactions between other Standard Model particles and the '*Higgs field*' via a process known as spontaneous symmetry breaking endows the property of mass to the other particles within the Standard Model [1–3]. Each particle within the Standard Model has an associated-anti particle, that is identical apart from opposite physical charges. However, some particles are their own antiparticle, such as the Higgs boson, photon, and gluon [4].

Fermions are spin 1/2 particles whose interactions are governed by the aforementioned force carriers. Each fermion comes in three *generations* whose properties are identical, apart from an increase in rest mass with each generation. For example, the electron has two counterparts– the muon (μ) and tau (τ), whose behaviour and quantum properties are identical, although mass increases by roughly 2 orders of magnitude between the muon and electron, and 4 orders of magnitude between the tauon and muon . The electron, muon and tauon each have a counterpart known as 'nuetrinos' (ν); extremely light weakly interacting fundamental particles with zero electric charge. The electron, and its subsequent generations, coupled with the electron neutrino and its subsequent generations are known as "leptons".

The final objects present within the Standard Model are quarks, and are also spin 1/2 fermions. Quarks come in two distinct types: up type and down type, which are characterized by their charge. Up-type quarks contain an electric charge of +2/3, and down type quarks have an electric charge of -1/3. Each type also comes in three distinct generations of increasing mass. Quarks combine together in groups of two or three to form *mesons* and *baryons*, respectively which are collectively referred to as *hadrons*. For example, protons contain 2 up quarks and 1 down quark, and neutral pions are comprised of one up quark and one anti– up quark. However, experimental efforts have recently discovered bound states of 4 and 5 quarks, although it is unclear if these are true hadronic structures, or 'molecules' of baryons and mesons [5, 6]. Quarks in hadronic matter are bound together by gluons, and are collectively referred to as *partons*. Although baryons and mesons consist of 2 or 3 *valence quarks*, a more complicated structure of hadrons arises through quantum fluctuations,

where quark-anti quark and gluon pairs are created from the vacuum [4]. Fig. 1.1 displays in tabular format the particles described by the Standard Model. A

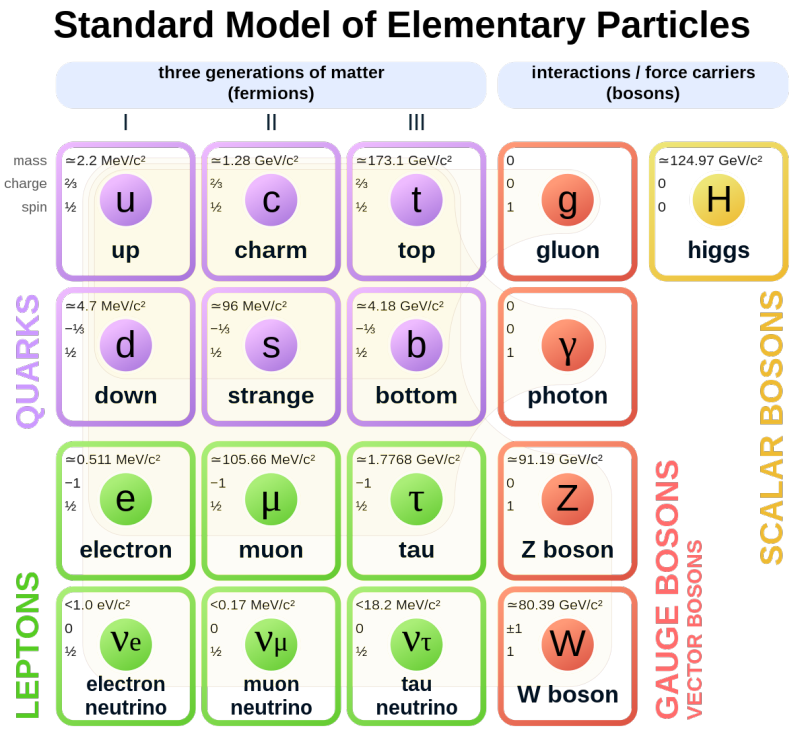

Figure 1.1: All Standard Model particles, including their spin, mass, and electric charge. The fermionic section displays the lowest mass generation in the leftmost column, and the highest in the rightmost column [7].

remarkable property of quarks is that they are never found alone in nature- i.e. if one quark strays too far away from another quark, it becomes energetically favourable to create another quark–anti quark pair from the vacuum, giving rise to the observation known as "colour confinement". This is due to a linear increase in potential energy at larger distances, and the process will be repeated ad infinitum in collider experiments as quarks are created following a collision of energetic initial particles, yielding characteristic 'jets' of hadrons.

1.1.1 *The strong force*

The strong nuclear force is one of the three fundamental forces of nature described by the Standard Model of particle physics. As its name suggests, it

is the strongest of the four fundamental forces and is responsible for binding hadrons and composite atoms together. Fig. 1.1 shows a table of the relative strengths of each fundamental force.

Force	Strength	Boson		Spin	Mass/GeV
Strong	1	Gluon	g	1	0
Electromagnetism	10^{-3}	Photon	γ	1	0
Weak	10^{-8}	W boson	$W^{\pm}$	1	80.4
		Z boson	Z	1	91.2
Gravity	10^{-37}	Graviton?	G	2	0

Table 1.1: Relative strength of each fundamental force, associated force carrier and their basic properties. Note the graviton is a theorized particle yet to be experimentally observed [8].

The strong force is described by SU(3) non-Abelian gauge theory; its Lagrangian is unchanged by local SU(3) gauge transformations. This ultimately manifests in three unique charges, referred to as "colour". These charges are analogous to the more intuitive 'electric' charge of electromagnetism, which is manifested theoretically through an Abelian U(1) gauge transformation of the corresponding quantum electrodynamics Lagrangian. All Lagrangians in the Standard Model are constructed respecting some local gauge symmetry, requiring them to be invariant under such a transformation.

A striking property of the theory of the strong force, known as quantum chromodynamics (QCD), is the running coupling constant, whose value scales inversely with energy scale (or equivalently, proportionately scales with separation distance between two strongly interacting objects) and is known as asymptotic freedom [9]. The coupling constant α_s, which determines the overall strength of the strong interaction, is also involved in the perturbative expansion procedure when performing QCD calculations at high energies. When $\alpha_s \ll 1$, the procedure is well defined and calculations can be explicitly computed up to arbitrary order. However, outside of this regime the standard approach of perturbation theory is not possible, and thus different approaches must be used, the standard technique being Lattice QCD (LQCD) [10]. This technique involves programming a discrete set of space-time points to tackle the incalculable path integrals encountered in QCD into a numerical computation [10]. LQCD predicts the production of the Quark Gluon Plasma at 150 MeV [11]. The major

drawback to such an approach is the computationally expensive nature of the calculations involved.

At high energies, the strong coupling constant becomes very small, and quarks forego their usual behaviour of colour confinement (known as *deconfinement*). In these conditions, that a new phase of matter consisting of unbound quarks and gluons is created known as the *quark gluon plasma* (QGP), which is thought to be present in the early universe one millionth of a second after the big bang. A collection of particle collider experiments around the world study the QGP in order to understand its properties and production.

1.2 QGP production in heavy ion collisions

The QGP can be created through high energy collsions of heavy ions. The highest energy collider experiments in the world are performed at the Large Hadron Collider (LHC), where lead (Pb) ions are collided in order to study the QGP. Two Pb bunches are accelerated to a significant fraction of the speed of light in opposite directions around a circular ring, which then intersect and collide at four distinct interaction points each housing a unique experiment. Due to their significant velocities, the ions are Lorentz contracted into 'disks' as viewed from the lab reference frame [12]. The amount of overlap between the colliding disks is parameterized by an impact parameter b, which is defined as the distance between the centres of the colliding objects. The nucleons that undergo an interaction are said to be 'participants,' and those outside of the overlap region are 'spectators' [12]. The resulting participant system is characterized by extremely high energy densities and temperatures and is where the QGP is thought to be created. Subsequently the system is subjected to rapid expansion and cooling. After sufficient cooling and expansion, the extreme energy densities are no longer present and the constituent quarks within the previously existing QGP resume their normal behaviour of confinement resulting in a process of hadronization [12]. After further expansion, the produced hadrons cease to interact with one another in a process known as *kinetic freeze out*. Fig. 1.2 illustrates the basic stages of a heavy ion collision. It can be seen here that the colliding nuclei are Lorentz contracted, due to the relativistic speeds at which

they are travelling. They subsequently expand, hadronize and freeze out as depicted from left to right.

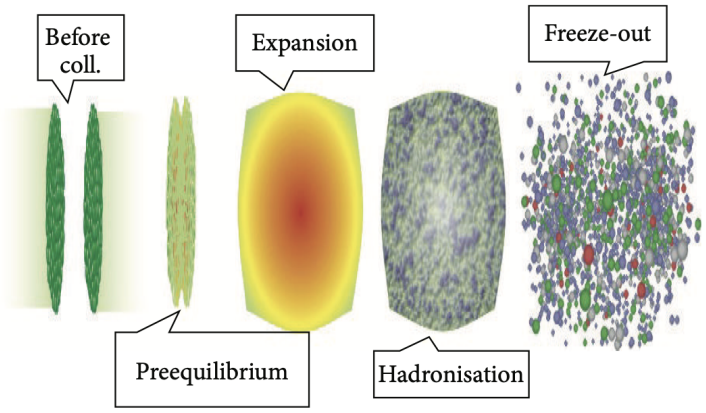

Figure 1.2: Basic stages of a heavy ion collision [13].

A heavy-ion collision can also be represented by a space-time diagram, shown in Fig. 1.3. If one lets $\tau = 0$ to be the time of collision, then prior to $\tau = 0$, the heavy ions are travelling essentially along the light cone. The subsequent

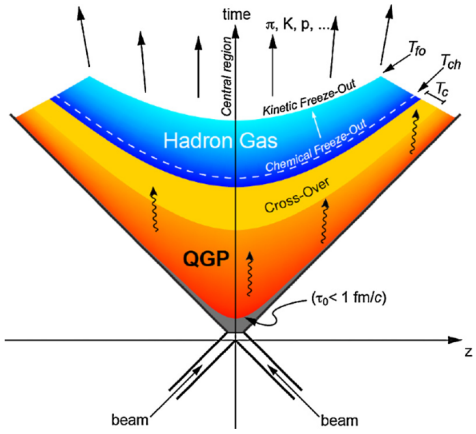

Figure 1.3: Spacetime diagram of a heavy ion collision [14].

stages are presented below [15]:

1. $0 \lessapprox \tau \lessapprox 0.2$ fm/c: Hard process dominant. Particles with high transverse momentum, p_{T} are created in this stage. This is constrained by the uncertainty principle, where reaction times are of order $1/Q$, with Q being

the transferred momenta. These particles are typically high momentum partons, direct photons, dilepton pairs, heavy quarks and vector bosons.

2. $0.2 \lessapprox \tau \lessapprox 1$ fm/c: Semi–hard processes. A large portion of the participant partons are freed. The partons then form a new ultra dense, non-equilibrium state, known as *glasma*. The quarks and gluons constituting the final state hadrons are produced here.

3. $1 \lessapprox \tau \lessapprox 10$ fm/c: QGP creation. Strongly interacting partons rapidly approach local thermal equilibrium, resulting in a high temperature phase known as the QGP. This results in a collective behaviour of the evolution of partons.

4. $10 \lessapprox \tau \lessapprox 20$ fm/c: Hadron gas. Local thermal equilibrium is still preserved. However, the QGP has undergone enough expansion and cooling to now be considered a hadron gas. The constituent hadrons interact with one another. 'Chemical freeze out' occurs when the composition of the hadrons ceases to change.

5. $\tau \gtrapprox 20$ fm/c: The system has lost a considerable amount of spatial density. The produced hadrons no longer interact with one another. The collision rate is slower than the rate of expansion.

QCD matter can be viewed in a phase diagram, shown in Fig. 1.4. Here, the phase diagram of QCD matter is presented in terms of the temperature (T) and baryon chemical potential (μ_B). In the $\mu_B = 0$ limit, there is an equal amount of baryons and anti baryons. When $\mu_B > 0$, there is a relative surplus of baryons to anfi baryons. The LHC provides ultra high energy collisions to create matter at high temperatures and low baryon chemical potential (equal amounts of matter and antimatter produced in a collision greatly outnumber the initial baryons). In this region, the transition between QGP and a hadron gas is a gradual crossover [12]. At lower energies encountered at the Relativistic Heavy Ion Collider (RHIC), μ_B is higher and the transition is a *first order* transition. The Beam Energy Scan at RHIC endeavours to find the 'critical point' at which the transition moves from a first order to gradual change in phase. Further studies to determine the critical temperature and (T_c) at which

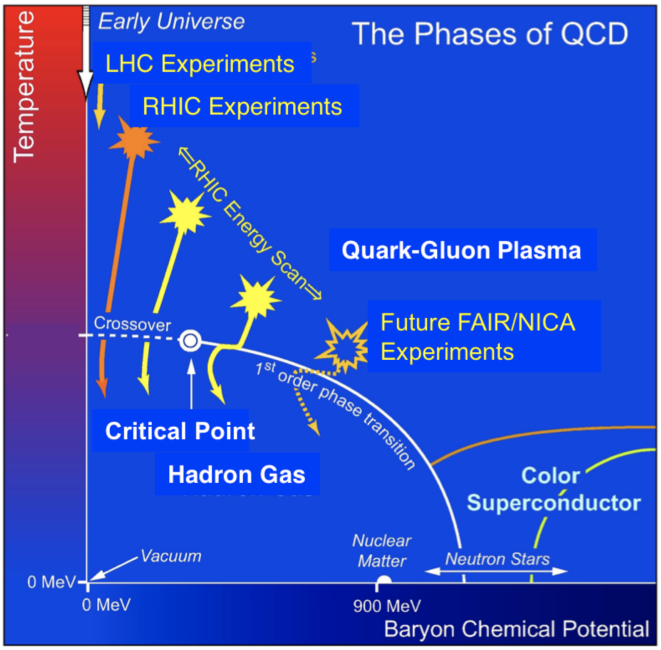

Figure 1.4: Phase diagram of QCD matter in the Temperature (T)–Baryon chemical potential (μ_B) plane. Experimental efforts and the region of the phase diagram which they study also presented [16].

the QGP transitions into a hadron gas have been calculated by LQCD to be 132^{+3}_{-6} MeV [17].

1.2.1 *Modelling heavy ion collisions*

Each distinct stage of a heavy ion collision must be modelled in order to predict how a final state will be observed experimentally. Experimental measurements can then be compared to models in an effort to interpret the physical observations. This is can be done by simulating initial conditions, QGP creation and expansion, and hadronic after- effects sequentially. Comparing various heavy ion observables to their theoretical description according to some model allows one to constrain properties of the initial conditions and QGP matter.

Initial conditions are required to have a mean p_{T} of zero within a local fluid element, since no one direction is preferred over another. Thus, any p_{T} dependence seen in the final state will be the result of an an intermediate hydrodynamic stage [18]. The QGP system can be modelled with relativistic hydrodynamics, which is dependent on the assumption that local thermal equi-

libium is preserved. This is particularly the case during the presence of QGP. Relativistic hydrodynamics obey the so– called ideal fluid equations [18]:

$$\partial^{\mu} T_{\mu\nu} = 0 \tag{1.1}$$

$$\partial^{\mu} j^{i}_{\mu} = 0, i = 1..M \tag{1.2}$$

where $T_{\mu\nu}$ is the energy momentum tensor, and j_{μ} is the (colour) charge current density.

1.3 Anisotropic flow in large and small systems

This section presents the key physics process pertaining to this work; *anisotropic flow*. It will be introduced in the context of large systems (Pb-Pb), and its presence in small systems (p-Pb) is then discussed. Physical interpretation of a flow signal in small systems is of significant importance within the field and is the subject of intense debate.

1.3.1 *Anisotropic flow*

The colliding Lorentz-contracted heavy ions can be geometrically thought of as as an overlap of two plates, resulting in an overlapping area often referred to as an 'almond shape'. The greater the degree of overlap between two collisions, the more the 'almond' resembles a circle, and has a small impact parameter (referred to as *central collisions*). Conversely, the lesser the degree of overlap, the colliding region geometry becomes more ovular. These collisions are called *peripheral collisions* and have a large impact parameter. Fig. 1.5 shows a simplified illustration of heavy ion collision geometry. Spectator particles are shown in blue, and participants are within the red *almond* with arrows indicating expansion. The impact parameter is shown alongside the x, y and z axes. The *reaction plane* (RP) is also shown defined as the plane of symmetry bifurcating the overlap region in the x-z plane. The QGP is thought to be created from the participant nucleons, and is azimuthally asymmetric due to the geometry of collision. Due to the spatial anisotropy, pressure gradients form within the QGP, with a larger gradient along the semi-minor axis in comparison to

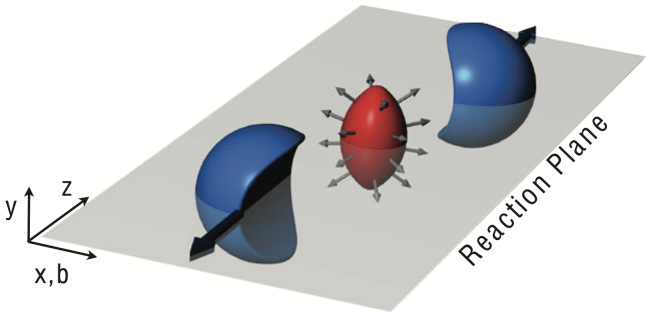

Figure 1.5: Heavy ion collision and geometry [19].

the semi-major axis. Pressure gradients obey thermodynamic behaviour which will translate the initial position space anisotropy into a final state momentum space anisotropy. This characteristic property of the QGP will then manifest with subsequent azimuthal anisotropic particle distributions. These distributions can be decomposed into a Fourier series in azimuthal angle, ϕ [20]. In an idealized picture as presented in Fig. 1.5, the purely ellipsoidal shape implies that only even terms relative to one common symmetry plane will be present in the expansion. However, event by event fluctuations force a more complicated structure in the Fourier series, ultimately manifesting in odd terms being non-vanishing and a unique symmetry plane for each order of the expansion, known as the *flow symmetry plane* (SP) [21]. Fig. 1.6 (a) shows a complicated collision geometry arising from fluctuations in the x-z plane. Fig. 1.6 (b) shows the collision geometry in the transverse plane, with the symmetry plane angle, Ψ_{SP}. Also shown is the *participant plane* (PP) angle, which is was used in previous pictures of heavy ion collisions. Mathematically, the azimuthal single particle distribution can be written as

$$\frac{dN}{d\phi} = 1 + \sum_{n=1}^{\infty} V_n e^{in\phi}, \tag{1.3}$$

where $V_n = v_n e^{in\Psi_n}$, is the 'flow vector' containing a flow magnitude v_n and flow symmetry plane angle Ψ_n. The flow magnitude v_n is a common observable used for the analysis of strongly interacting matter and can be expressed as $v_n = \langle \cos(n(\phi - -\Psi_n)) \rangle$, with angular brackets denoting an average over a set of collisions. Because flow measurements are driven by anisotropic initial

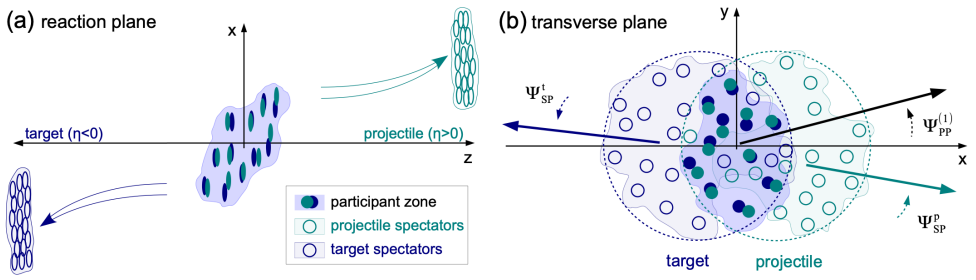

Figure 1.6: (a): Heavy ion collision geometry as viewed in the reaction plane. **(b):** Collision geometry as viewed in the transverse plane [22]. Geometric irregularities are the result of initial state fluctuations.

geoemetry (and also event by event fluctuations in the initial state), the more *eccentric* a collision is, the greater the value of v_n coefficients. The eccentricity corresponding to the n^{th} symmetry plane is expressed as [23]

$$\varepsilon_n = \frac{\int_{\boldsymbol{s}} e^{in\phi} |\boldsymbol{s}|^n \rho(\boldsymbol{s})}{\int_{\boldsymbol{s}} |\boldsymbol{s}|^n \rho(\boldsymbol{s})} \ , \tag{1.4}$$

Where $\boldsymbol{s}$ is a point within the overlap in the transverse plane, and $\rho(\boldsymbol{s})$ is the energy density profile in the transverse plane. Eccentricity can be related to centrality. Centrality can be determined by the number of particles produced in a collision (known as multiplicity). This is typically done by analyzing monte carlo studies where one can observe multiplicity as a function of centrality, in which multiplicity increases with the degree of overlap. The glauber model is the most commonly used study in this regard, which assumes that the constituent nucleons are moving in straight lines and are hard spheres distributed within the nucleus according to a Woods– Saxon distribution [24]. The nucleons are also treated as free particles [12].

1.3.2 *Flow in Pb–Pb collisions*

Anisotropic flow in heavy ion collisions has been studied extensively in particle collider experiments such as ALICE (A Large Ion Collider Experiment) and STAR (Solenoidal Tracker at RHIC). The flow magnitude v_2 is a common observable to quantify the degree of anistropy in azximuthal particle distributions. It can be expressed as a function of *centrality* (known as integrated flow)– the

degree of overlap between two colliding ions (which is expressed as a percentage of the most central collisions) as well as the transverse momentum (p_{T}) of the final state particles for a specific centrality (known as differential flow). The first measurements of v_n coefficients at the LHC are shown in Fig. 1.7, with integrated flow measurements on the left, and differential flow measurements on the right. As flow measurements become less central, the initial geometry becomes more eccentric, leading to higher pressure differentials within the medium and higher flow measurements. Data from experiment can then be compared to theoretical models including hydrodynamics with different initial condition parameters and properties of the QGP medium. Such comparisons allow one to constrain the QGP properties such as the shear viscosity (η/s) and bulk viscosity (ζ/s). In fact, the shear viscosity has been measured to be one half of the theoretical limit predicted using AdS/CFT techniques of $1/4\pi$, ultimately lending evidence towards the 'perfect fluid' interpretation of heavy ion data [25]. Fig. 1.8 shows a comparison of differential $v_2(p_{\mathrm{T}})$ for different centrality classes extracted by the ALICE collaboration with hydrodynamic models containing different initial conditions and shear viscosity values. It can be seen that different models describe the data with varying degrees of success. The models that describe the data best can then be used to parameterize the properties of the QGP.

1.3.3 *Flow in p–Pb collisions and tension with jet quenching*

While there is a considerable body of evidence (such as comparisons to hydrodynamic calculations) supporting the hypothesis that the QGP is created in Pb–Pb systems, it begs the question whether QGP formation could also occur in smaller collision systems. Originally, data from p–Pb collisions were used as a reference point to compare to heavy ion data. However, recent observations have recorded striking similarities between measurements in small systems and large systems.

A principle signature in Pb–Pb collisions (where the QGP is created) is the double ridge structure present in two-particle correlation functions (elaborated in section 2). This has also been observed in both p–p and p–Pb collisions and has generated significant interest. Fig. 1.9 shows the so called near and

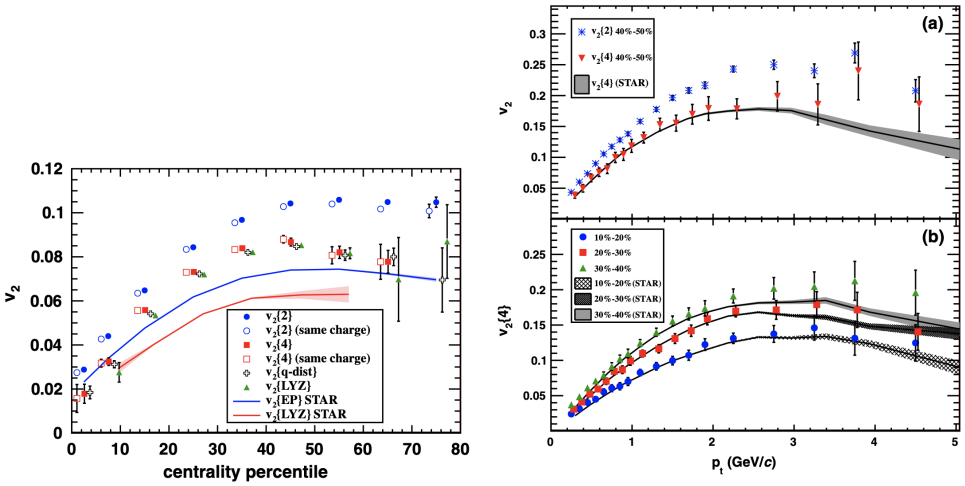

(a) Integrated v_2 with ALICE (points)compared to previous results from STAR (lines/shaded bands) the detector.

(b) ALICE recorded differential flow in different centrality ranges and compared to STAR experiment.

Figure 1.7: Integrated and differential flow as recorded by ALICE and STAR [26]. The number inside the curly brackets refer to different analysis techniques and will be expanded upon in Chapter 2.

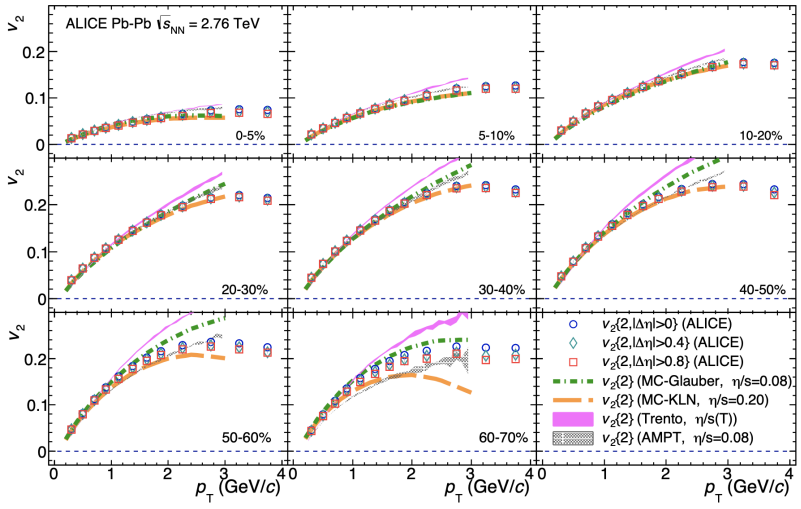

Figure 1.8: Experimentally observed v_2 in Pb–Pb collisions at $\sqrt{s_{\mathrm{NN}}} = 2.76$ TeV compared with theoretical models containing varying η/s and initial conditions (MC Glauber, TRENTO, MC-KLN, AMPT) [27].

away-side jet peaks in p–Pb collisions, reported by LHC experiments ALICE, ATLAS (A Toroidal LHC Apparatus), and CMS (Compact Muon Solenoid). Differential and integrated v_n coefficients can then be calculated from such two

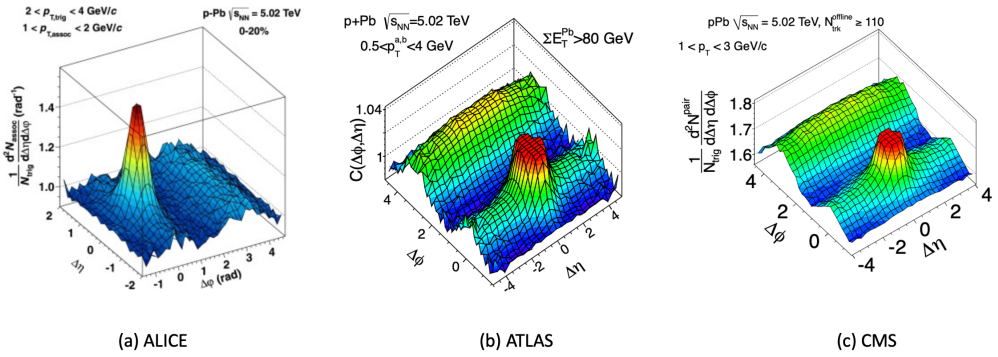

Figure 1.9: Double ridge structure in p– Pb collisions at 5.02 TeV observed by (a) ALICE [28], (b) ATLAS [29], (c) CMS [30].

particle correlation functions (see Chapter 2). It can be seen that v_2 is similar in Pb– Pb and p–Pb systems, with a saturation around 3 GeV/c and could be an indication of a common origin of the double ridge structure in all collision systems. At low p_{T} in Pb–Pb collisions, v_2 is consistent with a hydrodynamic interpretation. Moreover, v_3 between p–p and p–Pb are in very good agreement, and could be explained by hydrodynamics coupled with initial state event by event fluctuations. Fig. 1.10 shows v_2, v_3, and v_4 between different collision systems. The difference in v_2 in Pb–Pb is understood to be facilitated by the larger initial eccentricities driven by the collision geometry. It is important to note that because of the considerable differences in system size and geometries between small and large systems, no strong claims have been made regarding the creation of the QGP in small systems and requires further studies. The discovery of a flow signal in small systems whose origin is directly mediated by QGP creation and expansion would be a significant result, since such a process is not predicted by any fundamental theory. Furthermore, v_2 data has been shown to follow hydrodynamic calculations, particularly in high multiplicity classes, and lends further intrigue to the interpretation of small system collisions. Fig. 1.11 shows ALICE data in p–Pb compared to hydrodynamic calculations with $\eta/s = 0.08$ and Glauber Model initial conditions.

Although anisotropic flow measurement indicate agreement with hydrodynamic calculations, measurements of another phenomenon known as *jet quenching* may yield different interpretations. Jet quenching relies on the premise that produced jets interact strongly with the QGP medium, resulting in a suppres-

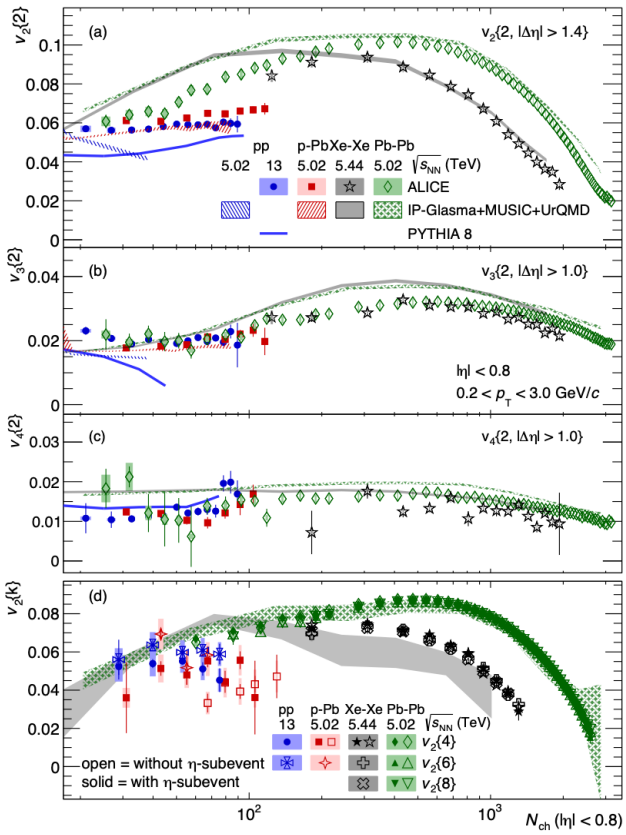

Figure 1.10: Integrated v_2 and higher order flow harmonics as reported by ALICE Pb–Pb, Xe–Xe, Pb–p, and p–p collisions at varying energies [31]. Also shown in the shaded bands are different theoretical models.

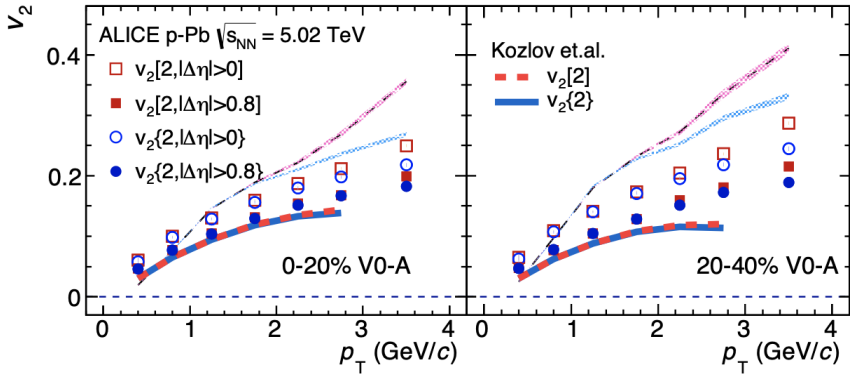

Figure 1.11: v_2 in p–Pb collisions at $\sqrt{s_{\rm NN}} = 5.02$ TeV. Dashed red line and solid blue line represent hydrodynamic modeling. Approximate agreement with data can be seen in the 0–20 % multiplicity class [27].

sion of their energy [32]. In small systems, a hypothetical droplet of the QGP would be much smaller than in large systems, implying that a traversing parton in a jet would lose significantly less energy. This would lead to the conclusion that a jet quenching phenomenon may not be measurable even if there is QGP creation. Fig. 1.12 shows the nuclear modification factor, ($R^{\mathrm{p-Pb}}$) as measured by ALICE. A deviation from unity in high p_{T} would indicate energy loss of a high p_{T} particle travelling through a QGP-like medium. It can be observed that ALICE data is consistent with unity. ALICE analysis of anisotropic flow and

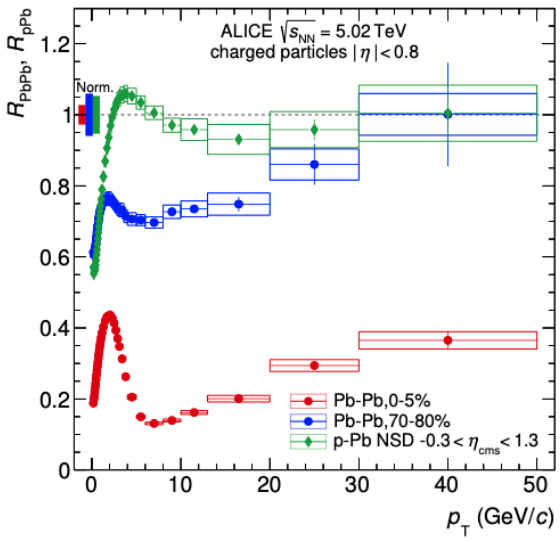

Figure 1.12: ALICE measurement of central (0-5%) $R^{\mathrm{p-Pb}}$ and and peripheral (70-80%) $R^{\mathrm{Pb-Pb}}$ at $\sqrt{s_{\mathrm{NN}}} = 5.02$ TeV [33].

jet quenching behaviour is seen to be in disagreement, with flow data having the potential to be interpreted from a hydrodynamic point of view. A resolution between the two methods of studying potential QGP production is needed. Moreover, the origin of a flow signal in small systems is not well understood and is the subject of increased study within the field of heavy ion physics. The emergence of a flow signal and collective effects such as the near side ridge in high multiplicity p–Pb collisions is a source of great intrigue, and a conclusive theoretical explanation of these effects is missing. The work presented in this thesis aims to gather evidence towards a possible explanation regarding the origin of a flow signal in p–Pb collisions at 5.02 TeV. The measurements performed yield constraints on future theoretical explanations of the observed phenomena.

This thesis is structured as follows: Chapter 2 introduces the phenomenon that is studied in this thesis, and the observables built to measure it. Chapters 3 and 4 outlines how the data is produced. Chapter 5 details how the data itself is analyzed in order to produce the desired observables. Chapter 5 also displays and discusses the results. Lastly, Chapter 6 offers a short conclusion and summary.

Chapter 2

Observables and non-flow

This chapter presents several flow observables that can be extracted experimentally, as well as the main concept behind this thesis - *flow vector fluctuations*. Methods of quantifying these fluctuations are then discussed, along with a short summary of the previous calculations performed in this area by ALICE. Non-flow contamination is then introduced, and a motivation for why these same calculations must be performed again with new techniques is lastly given.

2.1 Flow Observables

The symmetry plane angle in equation 1.3 is not experimentally accessible. However, Ψ_n can be approximated by averaging the azimuthal difference between particles over events. This is known as a *correlation*. The particle pair distribution can then be written as

$$\frac{dN^{\text{pairs}}}{d\varphi} = 1 + 2\sum_{n=1}^{\infty} v_n^2 \cos(n\Delta\varphi) = |V_n|^2 \ , \tag{2.1}$$

for all pairs of particles in a momentum region. This is known as a *two particle correlation*. A *cumulant* can then be calculated as

$$c\{2\} = \langle\langle \cos(n[\varphi_1 - \varphi_2]) \rangle\rangle \ , \tag{2.2}$$

where the brackets denote an average over particles and events and $[\phi_1 - \phi_2]$ is $\Delta\phi$.

The experimentally calculated value of differential flow coefficients $v_n(p_{\mathrm{T}})$ is frequently calculated from *two particle correlations*, where the azimuthal angle, φ of two particles found in a detector are compared [34]. It can be thought of as taking a ratio between two cumulants which subtracts particles from differing regions of p_{T} .

$$\begin{aligned} v_n\{2\}(p_{\mathrm{T}}) &= \frac{\langle\langle\cos[n(\varphi^{\mathrm{a}} - \varphi^{\mathrm{ref}})]\rangle\rangle}{\sqrt{\langle\langle\cos[n(\varphi^{\mathrm{ref}} - \varphi^{\mathrm{ref}})]\rangle\rangle}} \\ &= \frac{\langle v_n^{\mathrm{a}}(p_{\mathrm{T}}) v_n^{\mathrm{ref}} \cos[n(\Psi_n^{\mathrm{a}}(p_{\mathrm{T}}) - \Psi_n^{\mathrm{ref}})]\rangle}{\sqrt{\langle {v_n^{\mathrm{ref}}}^2\rangle}} \\ &= \frac{V_n^{\mathrm{a,ref}}}{\sqrt{V_n^{\mathrm{ref,ref}}}}, \end{aligned} \tag{2.3}$$

where the double angular brackets denote first an average over all particles in a collision, followed by an average over all events, and V_n is the experimentally measured *flow vector*. Here, the superscripts *a* and *ref* refer to the different ranges in p_{T} of which a particle is chosen from. A particle from the *reference particle group (ref)* belongs to the set of all particles originating from a large p_{T} range (in this thesis 0.2 - 3.0 GeV/c). On the other hand, a, refers to the group of particles belonging to a narrow p_{T} range. To calculate v_n for a particular p_{T}, the aximuthal angles of all the particles in a p_{T} range a are subtracted from the azimuthal angle of all the reference particles (excluding the instances where the it is the same particle in both sets). p_{T} dependence is observed after repeating the process for different values of a. It is also common to refer to particles from $p_{\mathrm{T}}^{\mathrm{a}}$ and $p_{\mathrm{T}}^{\mathrm{ref}}$ as *trigger particles* and *associate particles*, respectively.

A similar, yet distinct method of calculating v_n from particle correlations was developed in [35]:

$$v_n[2](p_{\mathrm{T}}) = \sqrt{\langle\langle\cos[n(\varphi^{\mathrm{a}} - \varphi^{\mathrm{a}})]\rangle\rangle} = \sqrt{\langle {v_n}^{\mathrm{a}2}\rangle} = \sqrt{V_n^{\mathrm{a,a}}}, \tag{2.4}$$

Here, both particles are taken from the same narrow p_{T} range, a, and the trigger and associate particle groups are identical. In other words, the sets of trigger and associate particles are identical. The disadvantage of such a calculation is since both trigger and associate particles are from a narrow p_{T} range, the

sample size is diminished, resulting in higher statistical uncertainties, which is most noticeable in the highest p_{T} bins.

Lastly one can create a comparison between sets of particles originating from unique p_{T} bins. The correlation in this case is thus

$$V_n^{\mathrm{a,b}} = \langle\langle \cos[n(\varphi^{\mathrm{a}} - \varphi^{\mathrm{b}})]\rangle\rangle = \langle v_n(p_{\mathrm{T}}^{\mathrm{a}}) v_n(p_{\mathrm{T}}^{\mathrm{b}}) \cos[n(\Psi_n(p_{\mathrm{T}}^{\mathrm{a}}) - \Psi_n(p_{\mathrm{T}}^{\mathrm{b}}))]\rangle. \quad (2.5)$$

Where $p_{\mathrm{T}}^{\mathrm{a}}$ and $p_{\mathrm{T}}^{\mathrm{b}}$ are separate p_{T} bins. In the case where $p_{\mathrm{T}}^{\mathrm{a}} = p_{\mathrm{T}}^{\mathrm{b}}$, equation 2.5 is equivalent to equation 2.4 squared. Note that although each case chooses particles differently, a two particle correlation is still performed. Thus, each technique represents an experimental measurement of the same observable, calculated using different sets of particles. Fig. 2.1 shows a sketch of how each correlator is calculated using different particle p_{T} selections. The reason for such selections will become apparent in Section 2.2.

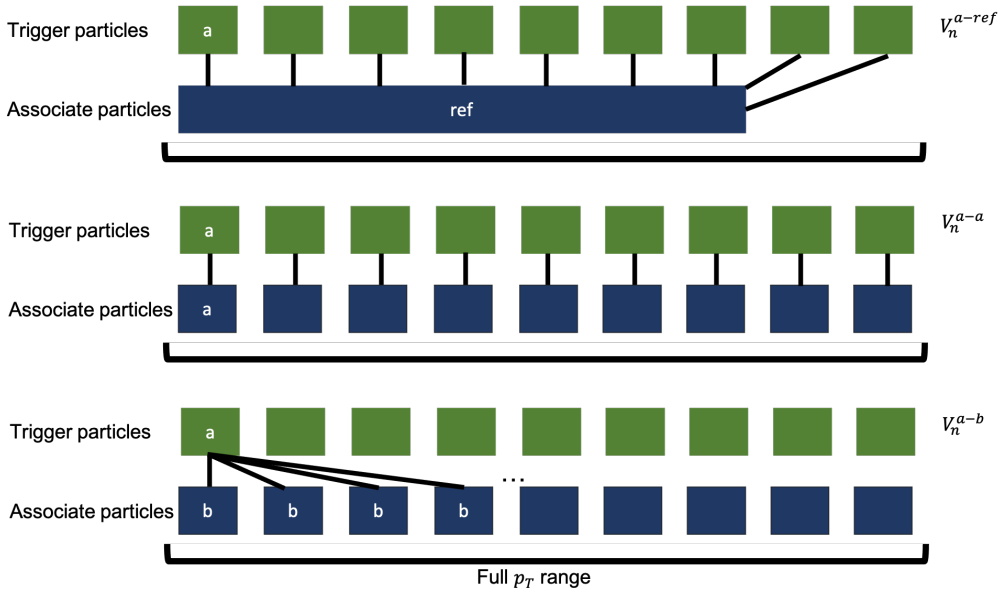

Figure 2.1: Different calculation techniques in two particle correlations. Connection lines in the last instance $V_n^{\mathrm{a,b}}$ are suppressed for simplicity.

2.2 Flow Vector Fluctuations

Due to event-by-event fluctuations in initial state energy density, hydrodynamic calculations showed that the flow vector V_n is thought to depend on transverse monentum, p_{T} [35, 36]. This indicates that either the flow magnitude v_n or the symmetry plane angle Ψ_n (or both) depend on p_{T} , i.e. $v_n = v_n(p_{\mathrm{T}})$ and $\Psi_n = \Psi_n(p_{\mathrm{T}})$ [37, 38]. Moreover, in Pb–Pb systems, such measurements have been used to constrain properties of the QGP such as the bulk viscosity [27]. Moreover, in the same study, an identical calculation was performed in small systems (p–Pb) and compared to hydrodynamic calculations, although no strong conclusions could be made because of non-flow (see section 2.3) contamination and large statistical uncertainties [27]. Thus, with improved study in small systems, measurements of flow vector fluctuations coupled with hydrodynamic calculations could possibly yield evidence towards the creation of the QGP in p–Pb collisions.

2.2.1 $\frac{v_n\{2\}(p_{\mathrm{T}})}{v_n[2](p_{\mathrm{T}})}$

One way of testing for flow vector fluctuations is by taking the ratio of equations 2.3 and 2.4 was proposed in [35]. In this ratio the numerator is affected by p_{T} dependent flow vector fluctuations, whereas the denominator is not. This can be seen in the construction if each observable; $v_n\{2\}(p_{\mathrm{T}})$ compares particles from a certain p_{T} range to a constant *reference flow*, whereas $v_n[2](p_{\mathrm{T}})$ compares particles from the same p_{T} bin. Thus, if p_{T} dependent flow vector fluctuations are present, they will manifest in $v_n\{2\}(p_{\mathrm{T}})$ since it is a p_{T} -wise comparison to a constant reference. In the case of $v_n[2](p_{\mathrm{T}})$, however, the comparison is between the same p_{T} intervals, meaning the fluctuations affect both trigger and associate particles equally, resulting in no sensitivity to flow vector fluctuations. Thus, taking the ratio between the $v_n\{2\}(p_{\mathrm{T}})$ and $v_n[2](p_{\mathrm{T}})$ will devolve from unity in the presence of flow vector fluctuations. Fig. 2.2 shows the previously calculated values for $\frac{v_n\{2\}(p_{\mathrm{T}})}{v_n[2](p_{\mathrm{T}})}$ in p–Pb collisions with ALICE at $\sqrt{s_{\mathrm{NN}}} = 5.02$ TeV compared to models with and without hydrodynamics. A deviation from unity can be observed that appears to follow hydrodynamic modelling presented in the blue line. A deviation from a model containing no

hydrodynamic behaviour (green shaded region) can is also seen in the most central collisions. However, due to no non-flow effects which must be controlled (see Section 2.3), a direct comparison of data to models does not provide any meaningful physics interpretation.

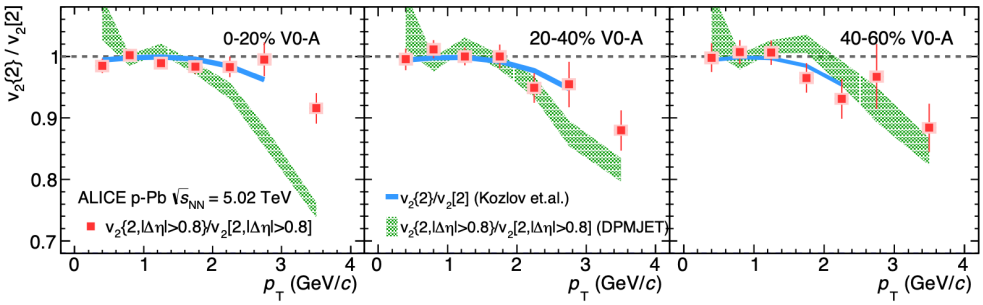

Figure 2.2: $\frac{v_n\{2\}(p_\mathrm{T})}{v_n[2](p_\mathrm{T})}$ as measured in [27] for different centrality ranges. The blue line represents hydrodynamic modelling (MUSIC [39]), whereas the green line indicates a model containing no hydrodynamics (DPMJET [40]).

2.2.2 r_2

Another measurement of flow vector fluctuations can be performed using the *factorization ratio* [36]:

$$\begin{aligned} r_n &= \frac{V_n^{\mathrm{a,b}}}{\sqrt{V_n^{\mathrm{a,a}} V_n^{\mathrm{b,b}}}} \\ &= \frac{\langle v_n(p_\mathrm{T}^\mathrm{a}) v_n(p_\mathrm{T}^\mathrm{b}) \cos[n(\Psi_n(p_\mathrm{T}^\mathrm{a}) - \Psi_n(p_\mathrm{T}^\mathrm{b}))]\rangle}{\langle \sqrt{v_n(p_\mathrm{T}^\mathrm{a})^2 v_n(p_\mathrm{T}^\mathrm{b})^2}\rangle}. \end{aligned} \tag{2.6}$$

As the name suggests, it is a test of the proposed factorization [41]:

$$V_n^{\mathrm{a,b}} = \langle\langle \cos[n(\varphi^\mathrm{a} - \varphi^\mathrm{b})]\rangle\rangle \stackrel{?}{=} v_n(p_\mathrm{T}^\mathrm{a}) \times v_n(p_\mathrm{T}^\mathrm{b}), \tag{2.7}$$

which was originally thought to hold under ideal hydrodynamic conditions due to independent emission of the particles from the medium [42–44]. However, current modelling instead predicts that factorization does not even hold under hydrodynamics due to fluctuations in the initial state [36]. Instead, r_n is constrained by the Cauchy inequality: $r_n \leq 1$. When $r_n = 1$, there is perfect factorization, whereas $r_n \leq 1$ suggests p_T dependent flow vector fluctuations

[36]. By definition, when $p_{\mathrm{T}}^{a} = p_{\mathrm{T}}^{\mathrm{b}}$, $r_n = 1$. Moreover, r_n provides detailed information on the p_{T} dependence of flow vector fluctuations, as it compares every possible p_{T} bin combination. The greater the difference between p_{T} bins, the greater a deviation from one is expected, as there is a greater decoherence resulting from initial state quantum fluctuations [36]. Fig. 2.3 shows the previously calculated values for r_2 in p–Pb collisions with ALICE at 5.02 TeV for different and p_{T} centrality ranges. A deviation from unity is observed in most ranges of $p_{\mathrm{T}}^{\mathrm{t}}$. The magenta line represents hydrodynamic modelling (MUSIC) with MC-Glauber initial conditions with $\eta/s = 0.08$. The red shaded region shows modelling containing no hydrodynamics (DPMJET). Agreement with hydrodynamic calculations is visible. However, as was the case in the previous section, a lack of non-flow suppression means that physical interpretation of the data is not possible when comparing to hydrodynamics. This will be discussed in the next section. Here, the notation p_{T}^{t} and $p_{\mathrm{T}}^{\mathrm{a}}$ is equivalent to $p_{\mathrm{T}}^{\mathrm{a}}$ and $p_{\mathrm{T}}^{\mathrm{b}}$.

2.3 Non-flow

Although there is previous ALICE study of $\frac{v_n\{2\}(p_{\mathrm{T}})}{v_n[2](p_{\mathrm{T}})}$ and r_2 in p–Pb collisions, it suffered from - large statistical uncertainties originating from a relatively small sample size in p–Pb run 1 ALICE data, and *non-flow contamination*. Non–flow contamination is the result of physics processes with a non–hydrodynamic origin. Process with a non hydrodynamic origin with different final state signatures will skew the final results. Examples of non flow contamination include jets and resonance decays [45]. These processes have the effect of producing small angles between φ_1 and φ_2 when constructing a correlator. In large systems is negligible in standard experimental analyses. In p–Pb, non - flow contamination plays a dominant role due to the lower multiplicities encountered, and was a major limiting factor in the p–Pb analysis in [27]. The previous study also used run-1 data, which suffered from large statistical errors. Thus, the work presented in this thesis was performed with the goal of improving upon the previously reported results of $\frac{v_2\{2\}(p_{\mathrm{T}})}{v_2[2](p_{\mathrm{T}})}$ and r_2 using larger sample sizes from run-2 data and state of the art non-flow subtraction techniques.

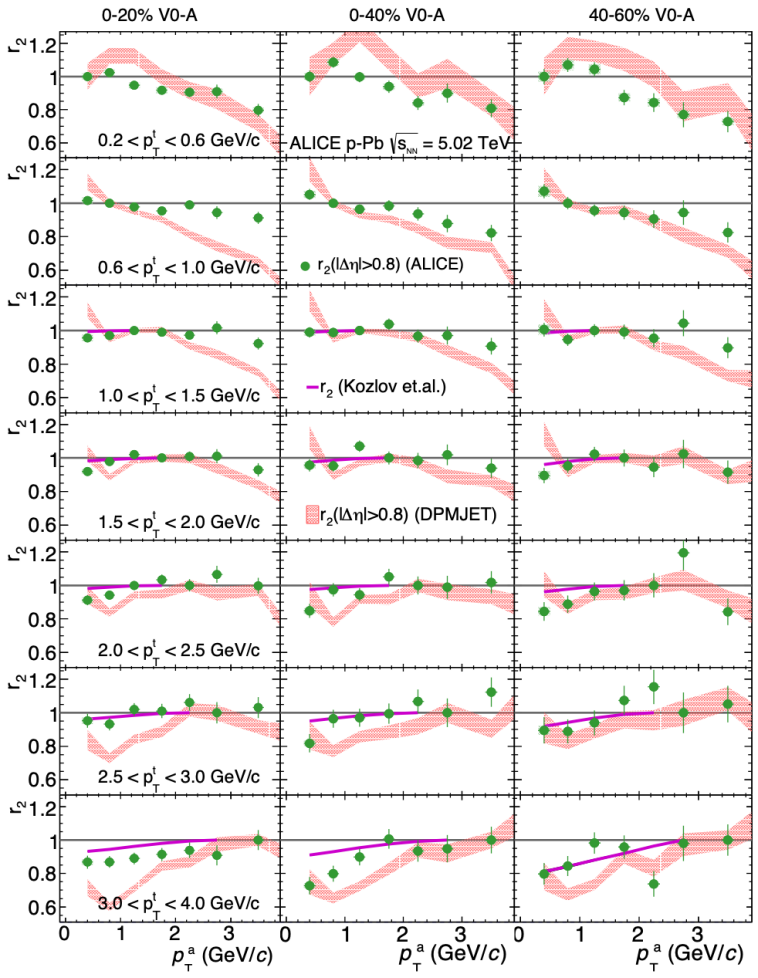

Figure 2.3: r_2 as measured in [27] for different centrality ranges. The magenta line represents hydrodynamic modelling with $\eta/s = 0.08$ (MUSIC [39]), whereas the red shaded line indicates a model containing no hydrodynamics (DPMJET [40]).

2.4 Dihadron correlations and non-flow

The central method used in extracting the final flow observables in this thesis is known as *dihadron correlations*, and is also a useful tool in illustrating non-flow processes. Through a series of operations described in Chapter 5, $\frac{v_n\{2\}(p_\mathrm{T})}{v_n[2](p_\mathrm{T})}$ and r_2 can be produced while suppressing non-flow in the process. Dihadron correlations are briefly introduced here in order to provide illustrations of flow and non-flow signals that can be observed in small systems.

A dihadron correlation selects two charged hadrons and calculates the rel-

ative difference in *psuedorapdity*, η azimuthal angle φ. Once $\Delta\varphi$ and $\Delta\eta$ has been calculated for each one particle relative to all the other particles registered in a particular event, the process is repeated for all remaining particles in the event (excluding auto-correlations). This is done for all events analyzed. Then, a histogram in $\Delta\varphi$ and$\Delta\eta$ can be produced, producing *correlation function*. Fig. 2.4 presents a typical correlation function encountered in this analysis after detector effects have been accounted for. Flow observables can be extracted from such correlation functions, and will be discussed in chapter 5, along with non-flow suppression strategies. However, signatures of flow and non-flow can be noted and discussed.

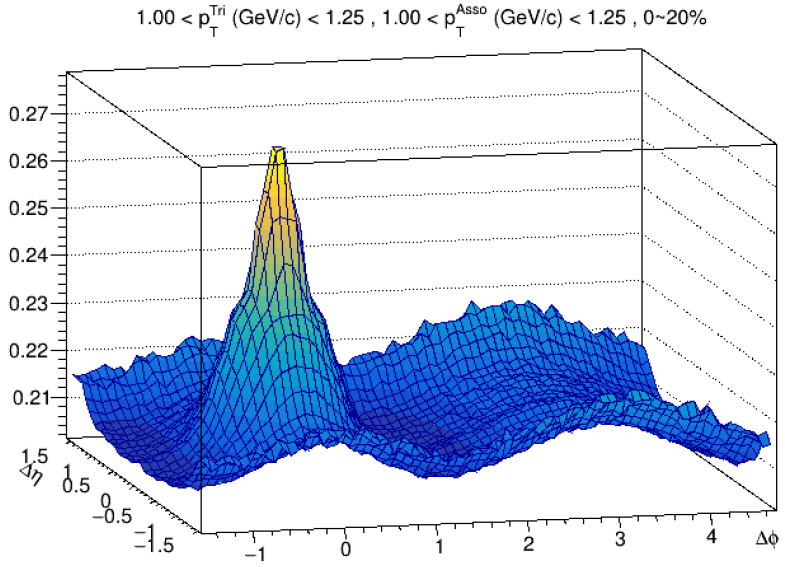

Figure 2.4: Correlation function produced after correcting for detector effects (see chapter 5 in p–Pb collisions at 5.02 TeV for $1.00 < p_{\mathrm{T}}^{a} < 1.25$ and $1.00 < p_{\mathrm{T}}^{b} < 1.25$ GeV/C in the 0 - 20 % centrality range, normalized by the number of trigger particles.

Two features are prominent in the example correlation function of Fig. 2.4: a noticeable 'peak' at $(\Delta\eta, \Delta\varphi) = (0,0)$, and a 'near side ridge' structure with maxima at $\Delta\varphi = 0$. The former is the result of jets causing a high number of short-range particles within the jet-cone, and is normally removed by projecting over a certain range $\Delta\eta$ values that exclude the region containing the so - called *jet peak*. The latter is a signature of flow in Pb–Pb, which was extensively studied in large systems, but was the source of surprise and excitement when

observed in small systems, which was first observed by CMS [46]. Physically, the near side ridge structure can be explained by collective effects occurring after a collision, and is a common argument for the creation of the QGP in A-A collisions [47], since collective effects are also predicted by hydrodynamic evolution. Collectivity is defined as the presence of long range angular correlations. The away-side ridge, however originates from correlations between a jet and recoil-jet and is observed regardless of the presence of flow. The double ridge structure is present across a number of small systems studied such as p-p, p-Al, p-Au, p-Pb, d-Au, and ^{3}He-Au [48]. However, multiple explanations have been put forward as to an explanation for the observed double ridge phenomena including collective hydrodynamic expansion [49], pomeron cascades [50], parton-jet interactions [51], and colour - glass condensate dynamics [52], among others [53–64] and requires experimental corroboration. This thesis seeks to build upon the evidence of a flow signal in p-Pb using the observables $\frac{v_n\{2\}(p_{\mathrm{T}})}{v_n[2](p_{\mathrm{T}})}$ and r_2 that quantify non-flow fluctuations described above.

Now that the field has been introduced, and the main quantities that evaluate flow fluctuations have been detailed, the following two chapters will highlight the apparatus used to collect the data involved in producing these calculations.

Chapter 3

Experimental Configuration and ALICE

This chapter explains the experimental apparatus used to record the data analyzed in this work. First, the large hadron collider (LHC) is introduced, followed by one of the four major experiments present on the LHC ring, ALICE (A Large Ion Collider Experiment). Lastly, the relevant subdetectors of ALICE are briefly discussed.

3.1 The Large Hadron Collider

The large hadron collider is a circular accelerator complex housing four unique experiments: ALICE, ATLAS, CMS, and LHCb [65]. Particles are accelerated in opposite directions in two separate rings to speeds close to the speed of light and brought to interaction points at interaction points located at each experimental complex. The LHC accelerates particles to the highest energies reached to date. Experiments conducted at the LHC fall under the umbrella term *experimental high energy physics*, although this term is not exclusive to just LHC energies. The LHC cavern is located roughly 100 m underground and lies on both French and Swiss territory, near Geneva, Switzerland. The 27 km circumference ring, which is in turn fed by smaller accelerator complexes to bring particles to their desired energies has to date completed two *runs* of data taking. During these periods, systems of p-p, p–Pb, Pb–Pb, and Xe–Xe

collisions have all been studied by all four LHC experiments. This study uses run-2 p–Pb collisions at $\sqrt{s_{\mathrm{NN}}} = 5.02$ TeV.

Acceleration is accomplished via a sequence of radio frequency (RF) pulses using instruments known as RF cavities, which are cooled to a superconducting state oscillating at 400 Hz [66]. The RF cavities are also responsible for sorting groups of particles at slightly different energies into 'bunches' of particles at the same energy. The particle beam must also be bent in order to follow the ring structure. This is accomplished by 8.3 T, 1×10^5 times stronger than the magnetic field of earth, superconducting dipole magnets of a 'twin bore' structure, where magnets for both beam rings are kept in the same low temperature environment or *cryostat*. This was forced from an engineering standpoint due to limited space [65]. Quadrupole magnets, among others, are also used to focus the beam. All magnets are kept at a temperature of 1.9 K with a liquid helium system in accordance with the requirements of the magnets' superconductivity.

3.2 ALICE

ALICE is a high energy particle detector built on the LHC ring. It is unique among the four main LHC experiments in that it is purpose-built for the study of heavy - ion physics. ALICE studies the properties QCD using a multitude of sub-detectors responsible for particle identification, tracking, and triggering, among others. Fig. 3.1 shows a schematic diagram of ALICE, with human shadows drawn for size comparison. The cylindrical portion is known as the *central barrel*, which contains several detectors built concentrically around the beam pipe, with a coverage of psuedorapidity $\eta < \pm 0.9$. The central barrel is kept inside a large solenoid magnet with a strength of 0.5 T. ALICE also has a forward portion known as the *muon arm* that covers a rapidity of $-4.0 < \eta < -2.5$. It measures leptons and contains a dipole magnet. The following sub-sections provide descriptions of the relevant detectors used in the analysis, and is referenced by [67].

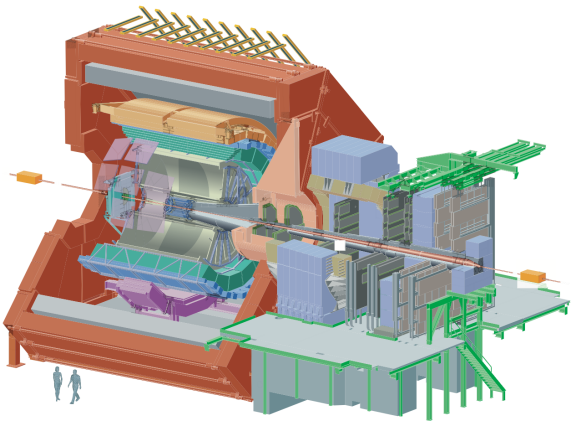

Figure 3.1: ALICE diagram [67]

.

3.2.1 *Inner Tracking System (ITS)*

The ITS is the innermost sub-detector in the central barrel and is thus the closest detector to the interaction point. It has the task of identifying the primary vertex of a collision with a resolution of μm. It also aids in identifying and tracking low energy particles of energies up to 200 MeV/c. It has 2π azimuthal angle coverage and η coverage up to $\pm$ 0.9, although the innermost layer provides coverage up to $\eta = \pm 1.98$. The ITS functions using six layers of silicon particle detectors, the first two of which are silicon pixel detectors (SPD), followed by two laters of siliocon drift detectors (SDD), and finally two layers of silicon strip detctors (SSD). The outer four most layers are responsible for particle identification, and use dE/dx measurements down to energies of roughly 100 MeV/c. The spatial resolution of the ITS is on the order of 10 μm, closest to the interaction point and decreases with radius. Spatial resolution is critical in determining precise momentum measurements at higher p_{T} .

3.2.2 *Time Projection Chamber (TPC)*

The TPC is the main detector in the central barrel. It has 2π azimuthal and $\eta < 0.9$ coverage, and is located directly after the ITS. It functions to provide maximum momentum resolution, particle identification, and two track separation at large multiplicities. The TPC is a drift gas detector that uses a mixture

of Ne-CO_2-N_2 gas and has a volume of roughly 90 m^3. Readings are made when an energetic particle strikes the gas inside the TPC cylinder, ionizing the gas and ejecting an electron. Electric fields situated along the z axis then direct the electron towards the endcaps of the TPC. The TPC is split into two equal parts by a high voltage electrode providing a highly uniform electric field of 400 V/cm throughout the volume of the cylinder. Readouts are found at the ends of detector, and is split into 18 trapezoidal sectors on either side of the TPC, where each trapezoid is divided into an inner and outer readout chamber. The readout chambers are designed to optimize momentum resolution for high momentum tracks. When a trigger is initiated, the gating grid opens after 6 μs for a period of roughly 90 μs, which is equivalent to the maximum time taken for an electron to traverse the medium. Due to the drift time of the electron-ion pairs, (80 μs), the maximum readout time of the TPC is 3 kHz. Fig. 3.2 shows a schematic drawing of the ALICE TPC.

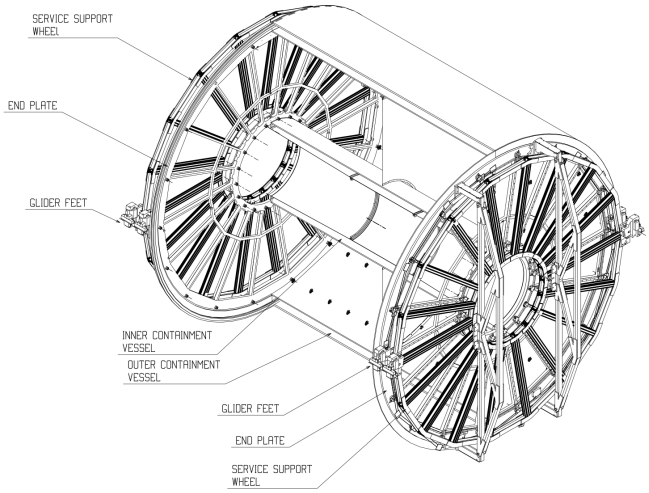

Figure 3.2: TPC schematic.

3.2.3 *V0*

The V0 system is a set of two detectors designed to supply trigger and multiplicity information for ALICE, and to distinguish between beam-beam interactions from background effects such as beam - gas interactions. The V0's also pro-

vide information pertaining to azimuthal angle distribution in a collision. They have a rapidity coverage of $2.8 < \eta < 5.1$ and $-3.7 < \eta < -1.7$, and are named V0A and V0C, respectively. V0C is located approximately 1 m away from the interaction point, and V0A is roughly 3.5 m away from the interaction point in the opposite direction. They are both arranged into 4 rings divided into 32 subsections composed of plastic scintillators that provide counting information. Fibre optic cables then transmit the light produced by the fibre optic cables into photomulitiplier tubes, which are then translated into a digital signal. The V0 are critical in constructing the minimum bias (MB) trigger that is used in this analysis. The V0 system is also responsible for the centrality estimation by measuring the charged particle multiplicity: $dN/d\eta$ by associating multiplicity with the total energy recorded by the scintillators. V0 amplitudes can then be compared to what would be expected by a Glauber distribution to estimate centrality. Fig. 3.3 shows a depiction of the V0 arrays.

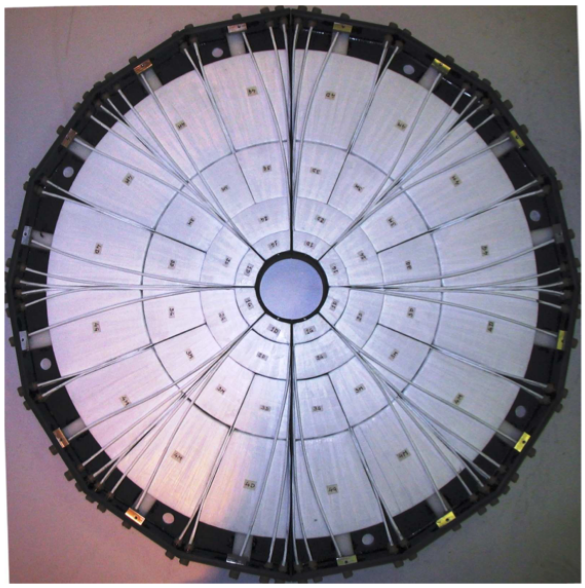

Figure 3.3: Photographic image of V0C used in ALICE

.

3.2.4 *Track Reconstruction*

The path a particle travels through the detector is also of experimental interest. A particle leaves a 'track' through the detector which can be measured, and is

known as *track reconstruction.* Individual points of data is first transformed into *clusters*, and a preliminary vertex is identified by maximizing the spatial point at which a maximal number of clusters converge upon. The ITS and TPC then find and fit the tracks using the 159 radially-stacked TPC pads. The TPC tracks are then propagated to the ITS, in which a number of candidate tracks in the ITS are calculated, from which the highest quality track is selected. The tracks are then inferred by comparison to the interaction point. Fig. 3.4 shows the steps involved in reconstructing a track with ALICE.

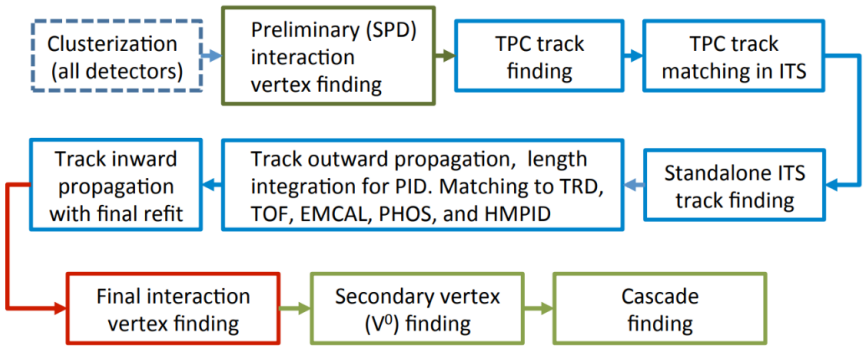

Figure 3.4: Steps involved in track reconstruction with ALICE.

3.2.5 *Triggering*

The ability to record all events is beyond current technological limits due to the very high interaction rate. Thus, automation is required to decide whether or not to record an event for analysis. This task is handled by the ALICE Central Trigger Processor (CTP), which is optimized for the different collision systems encountered at the LHC, and is divided into three levels of operation named L0, L1, and L2. The 'fast' trigger must be able to keep up with the high interaction rate in Pb-Pb collisions of 8 kHz, and is aided by L0 and L1. L0 reaches the detector in 1.2 μs, although it is too fast to signal all subdetector components. L1 arrives at 6.5 μs, and triggers remaining inputs. The final level, L2, arrives after 88 μs, to accomodate the drift time of the TPC in order to eliminate pile-up events. The information then feeds into the High Level Trigger system (HLT), which consists of 1000 microprocessor systems that further decides whether to

decide to keep an event, and which type of information to store depending on what is of interest. The final step is the digital acquisition system (DAQ) whose bandwidth of 1.25 GB/s ensures that events are properly moved to permanent storage. A number of trigger classes have been developed that modify the logic of L0, L1, and L2 and the HLT in order to collect and study events of varying interest and rarity. The minimum bias trigger used in this thesis is one of these classes, which has least stringent selection requirements.

Now that the relevant detectors have been introduced, the following chapter will discuss how data produced by the detectors is implemented into this analysis so that it can be calculated upon to produce $\frac{v_n\{2\}(p_{\mathrm{T}})}{v_n[2](p_{\mathrm{T}})}$ and r_2 .

Chapter 4

Workflow, Data, and Uncertainties

The following chapter details how the data was selected to produce the main results, and how the selected data was analyzed. The methodology involved in calculating both statistical and systematic error is lastly presented.

4.1 Workflow

CERN experiments use a purpose-built high-energy physics analysis framework known as `ROOT` [68], native to `C++`. Furthermore, ALICE utilizes extensions known as `AliPhysics` and `AliROOT` [69] in order to satisfy detector-specific needs within an ALICE analysis. `AliROOT` is composed of tools that any user might need in an analysis, such as event cuts. `AliPhysics` contains analyses used by individual users, and are stored as a class. The work in this thesis was performed using the class AliAnalysisCorrForFlow. The source code(and header file) can be found in the `ALICE GitHub` with path `AliPhysics/PWGCF/Flow/GF/AliAnalysisCorrForFlow.cxx(.h)`.

The basic workflow of the performed analysis is presented in Fig. 4.1. First, data from the detector is saved as an AOD (Analysis Object Data) file. An alternative to an AOD file is the ESD (Event Summary Data) file, although it has heavier memory demands. AODs however, contain less information but are sufficient for this analysis. The data is then read into the analysis task

mentioned above. Due to the large size of the data it is impossible to run a full analysis over the relevant data set locally. Thus, CERN has developed a grid service that runs analysis tasks on a number of off-site computing clusters that are powerful enough to process the large and complex data samples encountered in high energy physics analyses. It is best practice to only submit tasks with high memory requirements to the grid, and to do the remaining parts of the analysis locally. In this thesis, analysis was performed on the grid up to the point of producing the correlation functions, after which analysis was continued off-line. To further expedite the analysis process, the ALICE collaboration has developed the LEGO Trains system, which automates the grid submission procedure, and ensures that identical data sets are computed between tasks. For example, for various reasons - a sub-job might fail, which it then must be submitted for reprocessing. LEGO trains automate this process, and in the case of persistent failure, removes this sub-job from the other relevant tasks submitted to the train.

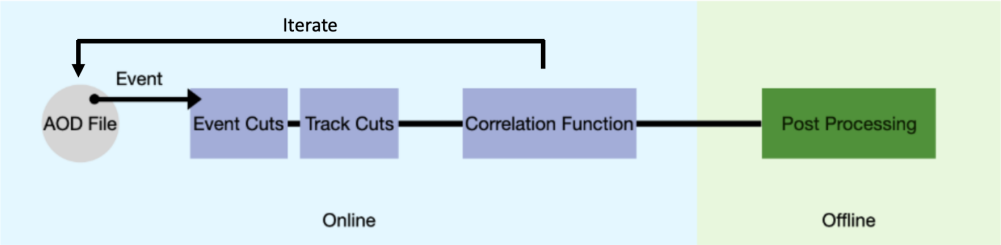

Figure 4.1: Analysis workflow. An event selected from an AOD file is analyzed. The process is then iterated for each event.

4.2 Data selection and detector corrections

Before any analysis is performed, a series of cuts must be applied to the data to ensure that only high quality, reliable sources of information are considered. Cuts are performed at the event level and then the level of individual tracks. This section presents the selection criteria used in this thesis. Furthermore, due to imperfections and nonuniformities in detector acceptance and efficiencies, corrections must be applied in order to achieve reliable results. These corrections are also described below.

4.2.1 *Data*

The data taken at the LHC is is firstly divided into *runs*. Runs are the periods of data taking between long shutdowns, in which upgrades to the LHC and its detectors are integrated, and no data is taken. To date, two runs have been recorded with run-3 expected to begin in 2022. This thesis deals with run-2 data, which had more collisions than in run-1. Runs are further divided into periods, which is characterized by the collision energy and particle species in the collision. The periods are further divided into *run-periods*, which is not to be confused with the previous definition. These runs correspond to periods of continuous data taking with the detector. This study analyzes data from the periods LHC16q and LHC16t, which is the time the p-Pb collisions at $\sqrt{s_{\mathrm{NN}}} = 5.02$ TeV were present in the LHC ring.

4.2.2 *Event cuts*

Events were selected according to the minimum bias (MB) trigger (in `AliPhysics`, this is labelled as *kINT7*). The signal amplitude of an event is estimated through AliMultSelection, with V0A as the detector responsible for centrality estimation. This detector is placed in the direction of the outgoing Pb particle after a collision, and is more reliable than using the V0C array, or both (V0M). This is only true in p–Pb collisions.

Furthermore, the lateral position primary vertex in the collision is restricted to be within 10 cm from the lateral central point of the central barrel. This is to ensure the relevant detectors 'catch' all the particles involved in a collision. If a collision occurs too close to the endcaps, then it will be likely that some particles will travel through points in which the central barrel has no coverage. The primary vertex is determined by the SPD, which is the central most detector and is closest to the interaction.

Due to the fast interaction rate present at the LHC, It can be very difficult to disentangle particles that are not from the same event. This is known as *pileup*. Pileup can occur in two types of instances: *in bunch* and *out of bunch* pileup. The former refers to when two particles from the same bunch collide, and are read by the detector as a single event. The latter refers to the situation when

collisions from two different bunches are registered in a single event. In either case, pileups can be identified by multiple primary interaction vertices in the event. Out of bunch cuts can further be identified by making cuts on correlations between the number of tracks between different detectors with readout times greater than the SPD readout time. This thesis uses the `AliPhysics` class `Physics Selection` to limit pileup. Table 4.1 shows the number of events analyzed after event cuts for each of the relevant centralities in this thesis, and the total number of events analyzed. In total, 46.7 million events passed event selction criteria and were analyzed in this work.

Centrality (%)	Number of events analyzed
0-20	1.65×10^7
60-80	1.59×10^7
80-100	1.43×10^7
Total:	4.67×10^7

Table 4.1: Number of events analyzed per centrality percentile used in this thesis. In total 46.7 million events fulfilled event selection criteria.

4.2.3 *Track cuts*

After events are properly selected, the individual tracks within an event are chosen according to a series of cuts. ALICE has developed a series of pre-set track cuts known as *filter bits*. In this analysis, Filterbit-96 is used for track selection. Filterbit-96 is also known as *global tracks*, since it uses information from multiple detectors. The cuts included in Filterbit 96 are:

- At least 70 TPC clusters registered
- One particle registered in the SPD, or if not, one particle registered in SDD.
- χ^2 per ITS cluster less than 36.
- χ^2 per TPC cluster less than 4.
- Distance of closest approach of the track to the primary vertex in the z direction less than 7 standard deviations.

- Distance of closest approach of the track to the primary vertex in the $x-y$ plane less than 2 cm.
- Track fit must converge during reconstruction.

Lastly, due to problems at the ends of the central barrel, only tracks within $|\eta| < 0.8$ are considered. Table 4.2 presents the main cuts used in this thesis, and Fig. 4.2 shows p_{T} and centrality sample distributions after cuts. Fig. 4.3 shows distributions in ϕ and η. Due to detector inefficiencies, there are some nonuniformities in ϕ and η that are corrected in chapter 5.

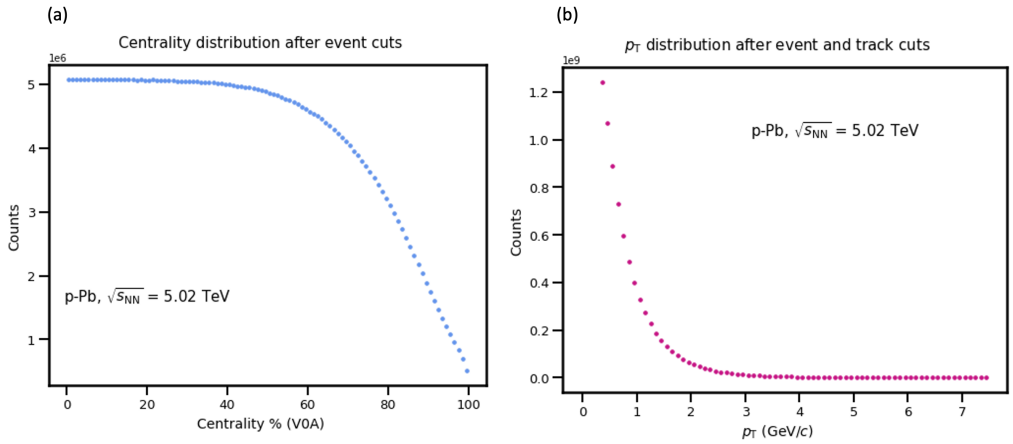

Figure 4.2: Sample distributions of p–Pb data at $\sqrt{s_{\mathrm{NN}}} = 5.02$ TeV for **(a):** centrality, and **(b):** p_{T} .

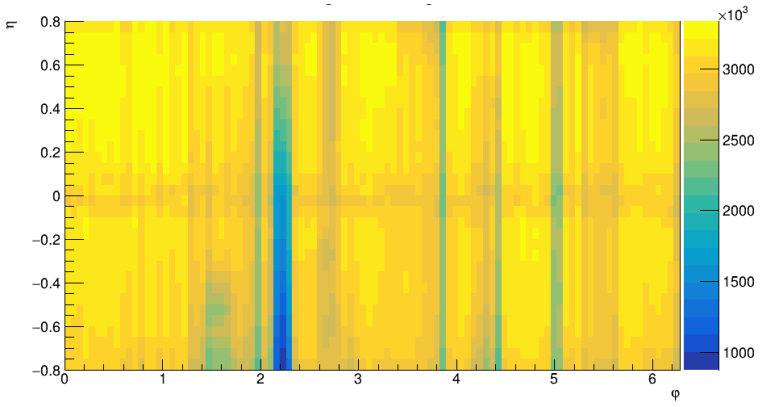

Figure 4.3: Sample distributions of p–Pb data at $\sqrt{s_{\mathrm{NN}}} = 5.02$ TeV for η and ϕ.

4.2.4 $\Delta\phi^*$ *considerations*

An important cut is made with respect to $\Delta\phi^*$. While two particles have a certain relative difference in azimuthal angle at the interaction point, as they travel through the magnetic field, they travel in arced paths resulting in a new angular difference in azimuth, known as $\Delta\phi^*$, and can be defined as

$$\Delta\phi^* = \phi_1 - \phi_2 + \arcsin\left(\frac{z \cdot e \cdot B_z \cdot R}{2p_{\mathrm{T}1}}\right) + \arcsin\left(\frac{z \cdot e \cdot B_z \cdot R}{2p_{\mathrm{T}2}}\right) , \qquad (4.1)$$

where ϕ_2 and ϕ_2 are the azimuthal angles of the particles at the interaction point, B_z is the magnetic field in the z direction, $p_{\mathrm{T}1}$ and $p_{\mathrm{T}2}$ are the transverse momenta of the measured particles, and R is the radius. Because of its resolution, the TPC can sometimes resolve two particles close together in $\Delta\phi^*$ as a single particle, or misread a single particle as two distinct particles. Thus, a cut of $\Delta\phi^* < 0.02$ radians at the radius of the TPC is applied.

Default Cuts	
Cut	Value
Primary Vertex	10 cm
Pileup	Physics Selection
DCA_{xy}	< 2.0 cm
DCA_z	$< 7\sigma$
# TPC Clusters	> 70
χ^2/TPC Cl.	< 4.0
χ^2/ITS Cl.	< 36
$\lvert\Delta\eta\rvert$	< 0.8

Table 4.2: Default event (green) and track (blue) cuts in analysis.

4.3 Uncertainties

4.3.1 *Statistical error and bootstrap*

Due to the nature of dihadron correlations, there is a significant amount of correlation between variables, making standard uncertainty analysis using propagation of error non-trivial. Thus, another way of estimating uncertainties is used. This analysis employs a bootstrap procedure to calculate uncertainties, which is a technique that relies on sub-samples of the main data set [70].

The pairs of particles contributing to the correlation function are assigned a random number between 0 and 9, forming 10 unique sub-samples of the main dataset. The relevant observables are then calculated for each sub-sample. Subsequently, a set of 100 samples are created from the sub-sample pool by randomly selecting 10 sub-samples and allowing for repetition. They were combined as a weighted average and the statistical uncertainty is then calculated as:

$$\sigma = \sqrt{\frac{\sum_{i=1}^{100}(w_i x_i - x)^2}{100 - 1}}, \tag{4.2}$$

where x_i are the values collected from the weighted averages, w_i is the inverse of the uncertainty squared extracted from the weighted averages, and x is the central value taken from the whole dataset without sampling. It is important to note that when $r_2 = 1$, the error computed by the bootstrap procedure is equal to 0. Due to the high memory constraints, a bootstrap is only performed for statistical uncertainties. Systematic studies are calculated using standard error propagation, and the ratio between bootstrapped and conventional errors are used as a correction factor when determining the significance of various systematic sources.

4.3.2 *Systematic errors*

A number of parameters in the analysis can be varied, such as the χ^2 per TPC cluster discussed above. For example, requiring a lower χ^2 per TPC cluster results in higher quality tracks, but reduces the sample size. Thus to ensure a robust analysis, it is necessary to change these parameters and quantify how much the final values change. If the results vary by a significant enough amount, then it is important to account for this in the final uncertainties, and is known as a systematic study. Table 4.3 shows the parameters varied and used in systematics in this work. The significance of systematic variations are determined via a Barlow test [71]. For each observable, the Barlow test

$$B = n\sigma = \frac{|x(p_{\mathrm{T}})_{default} - x(p_{\mathrm{T}})_{syst}|}{\sqrt{|\sigma^2_{default} \pm (\beta\sigma_{syst})^2|}} \tag{4.3}$$

Cut	Default Value	Systematic Value
Primary Vertex	< 10 cm	< 7 cm
$\|\Delta\eta\|$	< 0.8	$< 1.0, 1.2$
Filterbit	96	768
# TPC Clusters	> 70	> 90
χ^2/TPC Cl.	< 4.0	< 3.0

Table 4.3: systematic variations in event selection (green), analysis analysis method (yellow), and track selestion (blue).

counts the number of standard deviations a systematic variation is away from the default value for each p_{T} . In the denominator, a negative sign is used if the systematic data sample is a subset of the default data set, and is positive if otherwise. Here, $x(p_{\mathrm{T}})$ is the the central value from the default and systematic cuts, and σ is the standard deviation. Memory allocation constraints make it unfeasible for a bootstrap procedure to be performed for systematic analysis, which would require a memory heavy sub-sampling procedure for each systematic analysis. Since there is no bootstrap in the uncertainty of systematic error, $\beta = \sigma_{bootstrap}/\sigma_{prop}$ is used as a correction factor to scale the uncertainties calculated with systematics, where σ_{prop} is the uncertainty derived from standard propagation of error techniques. A critical assumption in incorporating β is that there is a linear scaling between the traditionally calculated uncertainty and the bootstrap uncertainty. The barlow value is averaged over p_{T} bins. If the value is greater than unity, a first degree polynomial fit is performed over the ratio between the default value and systematic value, and the uncertainties are calculated by the absolute value of the difference the fit from 1 with each p_{T} bin. The systematic uncertainties that pass the barlow test are then added in quadrature in order to procure a final systematic error.

The following chapter will finally explain how the implemented data is analyzed to produce $\frac{v_n\{2\}(p_{\mathrm{T}})}{v_n[2](p_{\mathrm{T}})}$ and r_2 , and how detector effects are accounted for. It also reports the main results of this thesis.

Chapter 5

Analysis Details and Results

Ultra-relativistic heavy ion collisions at the LHC create the low baryon chemical potential and high temperatures required to produce the quark gluon plasma. Collisions of smaller systems are not believed to be able to create the conditions necessary for quark gluon plasma formation. However, measurements of anisotropic flow observables and the observation of a double ridge structure suggest reveal similarities between the two systems that were not predicted, and an explanation regarding manifestation of a flow signal in p–Pb is required. Through dihadron correlations, flow vector fluctuations in high multiplicity p–Pb collisions at $\sqrt{s_{\mathrm{NN}}} = 5.02$ TeV can be measured while also suppressing non-flow signals. Production of such measurements can offer comparisons to theoretical models hoping to describe these phenomena in an effort to seek the underlying physical mechanism responsible for producing such signals.

The previous chapters have outlined the motivations and experimental technique used to perform this analysis, and the observables to be calculated. This chapter outlines how data measured by the detector is used to produce the flow observables. The two main techniques of non-flow subtraction are introduced: *peripheral subtraction* and the *template fit*. From these techniques flow observables are produced in which non-flow will be suppressed. Comparisons between the two methods are made and discussed. An overview of the systematic uncertainty is also shown. Lastly, final results of $\frac{v_2\{2\}(p_{\mathrm{T}})}{v_2[2](p_{\mathrm{T}})}$ and r_2 are given, and their physics implications towards the existence of flow vector fluctuations and theoretical constraints are discussed.

5.1 Dihadron Correlations

Dihadron correlations (correlation functions) are produced by iterating over each particle, and calculating $\Delta\eta$ and $\Delta\varphi$ relative to every other particle found in an event. Two-dimensional histograms are then produced according to the trigger - associate particle prescription in Fig. 2.1, which is important when constructing the relevant observables $\frac{v_n\{2\}(p_T)}{v_n[2](p_T)}$ and r_2 . Fig. 5.1 shows a correlation function for $1.50 < p_T^a < 1.75$, $1.50 < p_T^b < 1.75$ GeV/c, at 60–100% centrality, which will in the end aid in producing $v_2[2](p_T)$ and r_2 . However, note that as $|\Delta\eta|$ increases, there is a strong decrease in the histogram count. This is the product of the combinatorial background that is implicitly introduced when performing correlations in the same event.

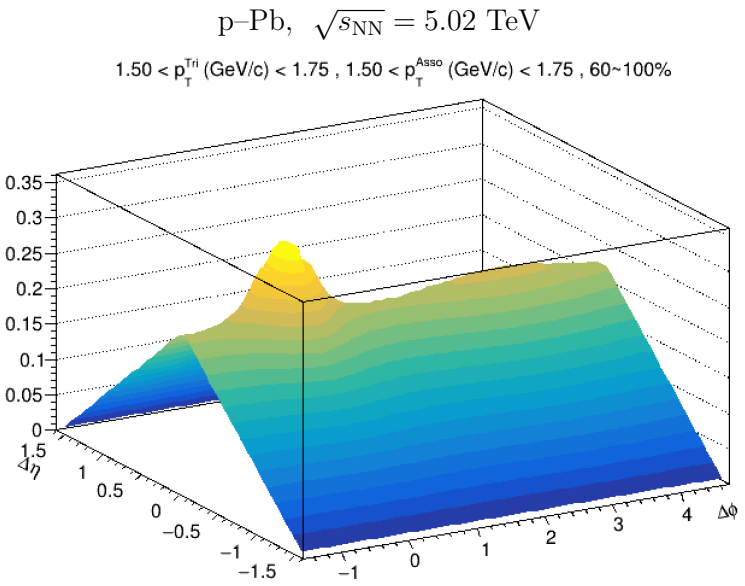

Figure 5.1: Correlation function for p–Pb collsions at $\sqrt{s_{NN}} = 5.02$ TeV from the same event for $1.50 < p_T^a < 1.75$, $1.50 < p_T^b < 1.75$ GeV/c. 60–100% centrality, normalized by the number of trigger particles.

5.2 Event Mixing

Fig. 5.1 presents a problem not currently addressed: combinatorial background at the lateral periphery of the TPC. This problem is rectified by an *event mixing*

procedure [72], which will also correct for geometry-wise detector acceptance inefficiencies. In the event mixing procedure, trigger particles from one event are correlated with associate from particles from a separate event. Since particles from separate events are not correlated, a correlation function produced this way will not contain any 'physics', but only acceptance effects produced by the detector. This is called the *mixed event* or *background* correlation function, whereas correlation functions produced from the same events are called the *signal*. In order to ensure that the same levels of particles are compared between p_{T} intervals, the signal events are normalized by the number of trigger particles, N_{trig}, and produce the *signal* correlation function $S(\Delta\eta, \Delta\varphi)$:

$$S(\Delta\eta, \Delta\varphi) = \frac{1}{N_{trig}} \frac{d^2 N_{same}}{d(\Delta\eta)\ d(\Delta\varphi)} \tag{5.1}$$

When constructing correlation functions for calclating r_2 , however, a different normalization must be used. Since there is no difference apart from the label of *trigger* and *associate* in this specific case, it should be expected that r_2 is symmetric under permutations of $p_{\mathrm{T}}^{\mathrm{a}}$ and p_{T}^{b}. However, this permutation would then cause a different number of trigger particles. In order to keep the normalization invariant under permutations of $p_{\mathrm{T}}^{\mathrm{a}}$ and p_{T}^{b}, the signal correlation function is normalized as

$$S(\Delta\eta, \Delta\varphi) = \frac{1}{N_{trig} \cdot N_{asso}} \frac{d^2 N_{same}}{d(\Delta\eta)\ d(\Delta\varphi)} \tag{5.2}$$

instead. Similarly, the correlation function, $B(\Delta\eta, \Delta\varphi)$ is defined as:

$$B(\Delta\eta, \Delta\varphi) = \frac{1}{\alpha} \frac{d^2 N_{mixed}}{d(\Delta\eta)\ d(\Delta\varphi)}, \tag{5.3}$$

where α is the integral along a narrow region in the $\Delta\varphi$ plateau:

$$\int_{-\pi/2}^{3\pi/4} \int_{-0.02}^{0.02} B(\Delta\eta), \Delta\varphi)\ d(\Delta\eta) d(\Delta\varphi), \tag{5.4}$$

where the integration excludes the nonuniformity around $\Delta\eta \approx 0$ that arises from the $\Delta\phi^*$ cut described in section 4.2.4, which eliminates some particles that would otherwise be present. However, these cuts must also be implemented in

the mixed event histograms so as not to introduce a bias. This normalization factor can be defined in a number of different ways, although the different definitions have a negligible impact on any final calculations. The factor of α is added in order to sure that similar multiplicities between the signal and background are compared. Furthermore, signal events are only correlated with mixed events with suitable centrality, p_{T} , and z vertex. Fig. 5.2 shows a correlation function produced through the event mixing method. Since particles from different events will not have any correlation, no physics effects are seen in mixed correlation functions. The correlation function corrected for geometric

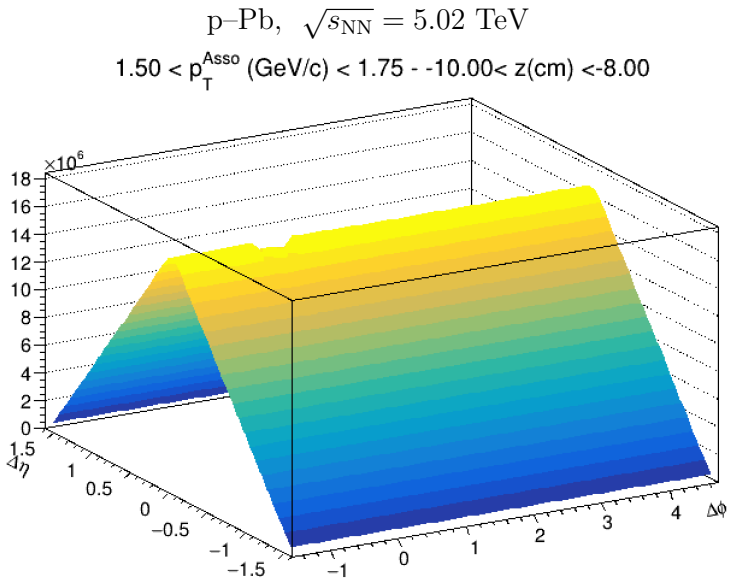

Figure 5.2: Mixed correlation function in p–Pb collsions at $\sqrt{s_{\mathrm{NN}}} = 5.02$ TeV for $1.50 < p_{\mathrm{T}}^{\mathrm{a}} < 1.75$, with z vertex from -10 to -8 cm. This function only carries information about geometry - wise detector effects.

detector effects, $C(\Delta\eta, \Delta\varphi)$, can then be calculated by

$$\frac{1}{N_{trig}} \frac{d^2 N_{pair}}{d(\Delta\eta)\, d(\Delta\varphi)} = \frac{S(\Delta\eta, \Delta\varphi)}{B(\Delta\eta, \Delta\varphi)} = C(\Delta\eta, \Delta\varphi) \ . \tag{5.5}$$

Following this procedure, a correlation function that is free of geometric detector effects and a combinatorial background can the be produced, for example as in Fig. 5.3. The sharp decrease in $\Delta\eta$ has been eliminated, and a near side ridge has appeared. A similar ridge has been observed in large systems, and can be

explained by the presence of the QGP Although some detector inefficiencies

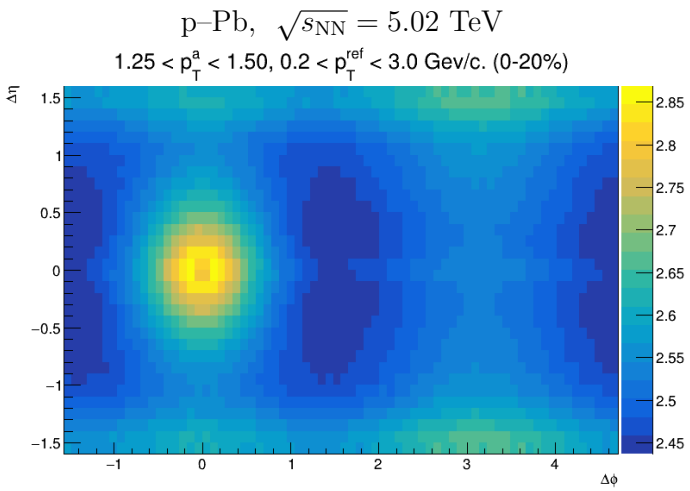

Figure 5.3: Heat-map of the corrected correlation function for $1.25 < p_{\mathrm{T}}^{\mathrm{a}} < 1.50$, $0.2 < p_{\mathrm{T}}^{\mathrm{ref}} < 3.0$. Even before the suppression of non-flow, a near side ridge is seen, and is a sign of collectivity in p–Pb collisions, which was an unexpected observation when first noticed.

have now been accounted for, it is also important to account for p_{T} dependent inefficiencies, which will be addressed in section 5.3.

5.3 Efficiency correction

Detectors in the central barrel also suffer from p_{T} dependent inefficiencies, resulting in inaccurate single-particle p_{T} distributions. In order to correct the data to represent reality, simulation driven corrections must be applied. In such a correction, physics events are produced in a simulation twice: once without a detector, and once again simulating the same events and particles travelling through a detector (usually simulated by GEANT-4 [73]). The ratio between the number of particles produced in in a simulated collision ($N_{generated}$) relative to the number of particles measured by a simulated detector ($N_{reconstructed}$) can then provide a p_{T} dependent correction to be applied to data.

Efficiency corrections have already been produced by the ALICE collaboration for the periods studied in this thesis, so an original production of efficiencies by the author was not necessary, and was only a matter of implementation. Efficiencies were simulated using DPMJET [40], after which an efficiency coefficient,

ε can be calculated as

$$\varepsilon(\text{centrality}, p_{\mathrm{T}}, \eta) = \frac{N_{reconstructed}}{N_{generated}} \ . \tag{5.6}$$

ε can then be assigned as a particle weight when constructing the correlation function as:

$$S(\Delta\eta, \Delta\varphi)_{true} = \frac{1}{\varepsilon_{trigger} \cdot \varepsilon_{associate}} \ S(\Delta\eta, \Delta\varphi)_{measured} \ . \tag{5.7}$$

Additionally, the number of trigger particles must also be scaled as

$$N^{trigger}_{true} = \frac{1}{\varepsilon} \ N^{trigger}_{measured} \ . \tag{5.8}$$

Efficiencies are calculated to be centrality and p_{T} dependent. Furthermore, since p–Pb is an asymmetric system, efficiencies also must be calculated as a function of psuedorapidity. Fig. 5.4 depicts ε as a function of p_{T} and centrality in the central most psuedorapity range, $|\eta| < 0.2$. Lastly, in the consideration of systematics, customized simulations have been produced considering each systematic variation.

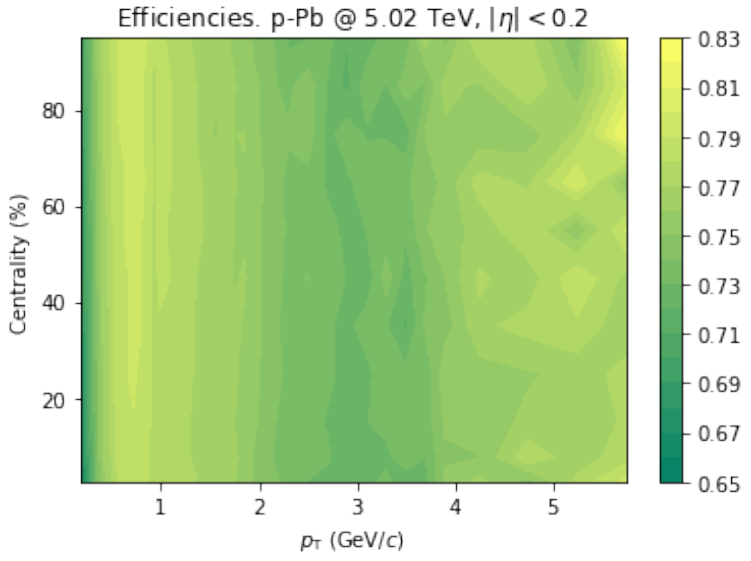

Figure 5.4: Efficiency plot (ε) for p–Pb collisions at $\sqrt{s_{\mathrm{NN}}}$= 5.02 TeV as a function of centrality and p_{T} , which is subsequently used as particle weights.

Although it is important to correct for such effects, since the final observables calculated in this thesis involve fractions of correlations, the p_{T} dependent effects in efficiency corrections largely cancel, making the final effect negligible. However, for the sake of accuracy and correctness efficiency corrections have been applied throughout this analysis.

5.4 Non-Flow Suppression and Extraction of Flow Observables

Previous study has indicated the need for controlling non-flow effects when calculating $\frac{v_n\{2\}(p_{\mathrm{T}})}{v_n[2](p_{\mathrm{T}})}$ and r_2 in p-Pb collisions [27]. This section presents the two independent methods used in this thesis to control non-flow and finally calculate $\frac{v_n\{2\}(p_{\mathrm{T}})}{v_n[2](p_{\mathrm{T}})}$ and r_2 .

5.4.1 *Peripheral subtraction*

Peripheral subtraction relies on the assumption that high multiplicity collisions in small systems contain a significant amount of 'flow', whereas low multiplicity collisions are purely non-flow. This can be supported by comparing a high multiplicity correlation function to its low multiplicity counterpart. In the high multiplicty regime, the double ridge structure is clearly visible to the naked eye, whereas the ridge is not visible in low multiplicity collisions. This is illustrated in 5.5 (a) and (b), which shows collisions from 0-20% centrality and 60-100% centrality, respectively. Here, an away side ridge is observed in both cases, which is the result of correlations between jet particles with recoil jet particles. The near side ridge is predicted by collective effects that could be produced by hydrodynamic expansion.

Low multiplicity correlation functions can be subtracted from high multiplicity correlation functions, effectively 'subtracting away' non-flow. The result is a subtracted correlation function with suppressed non-flow effects, as shown in Fig. 5.6. Note that despite subtraction, a noticeable jet-peak is still present. This thesis uses high multiplicty collisions as 0-20% centrality, and low multiplicity collisions as 60-100% centrality.

After the subtraction procedure, experimental values can now be extracted

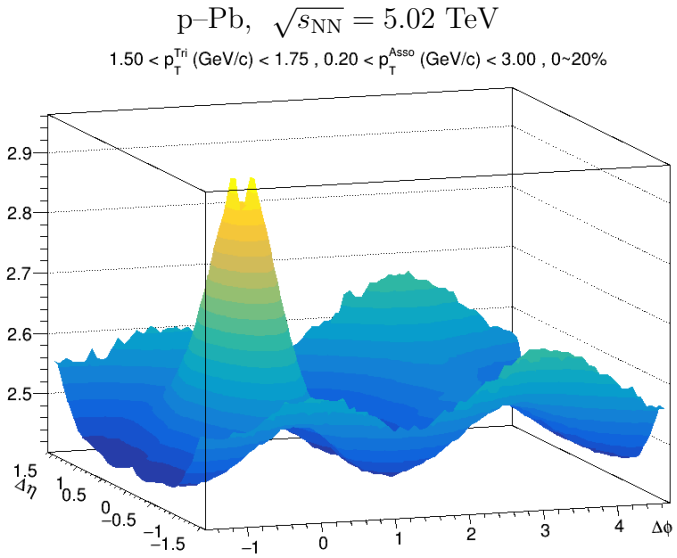

(a) High multiplicity: 0-20% centrality

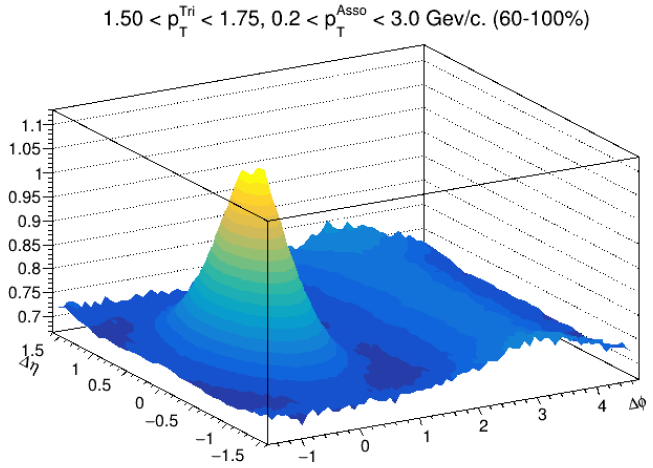

(b) Low multiplicity: 60-100% centrality

Figure 5.5: (a): High multiplicity and **(b)**:low multiplicity p–Pb collisions at $\sqrt{s_{NN}} = 5.02$ TeV. The 'near side ridge' is not discernible in **(b)**.

from the correlation function that are less contaminated by non-flow effects. First, the histogram is projected onto the $\Delta\varphi$ axis. Since there still exists a jet peak, points falling within $|\Delta\eta| < 0.8$ are excluded from the projection. The projected histogram is then fit with the first 3 terms of the fourier series

approximating the angular distribution in $\Delta\varphi$:

$$f(\Delta\varphi) = a_0 + 2\sum_{n=1}^{3} a_n \cos(n\ \Delta\varphi). \tag{5.9}$$

Where a_n are fit parameters and the fit is performed via a minimization of χ^2. The correlators can then be extracted by

$$V_{n\Delta} = \frac{a_n}{a_0 + b}, \tag{5.10}$$

where Δ indicates that a gap in $\Delta\eta$ has been applied. Here, a correction factor,

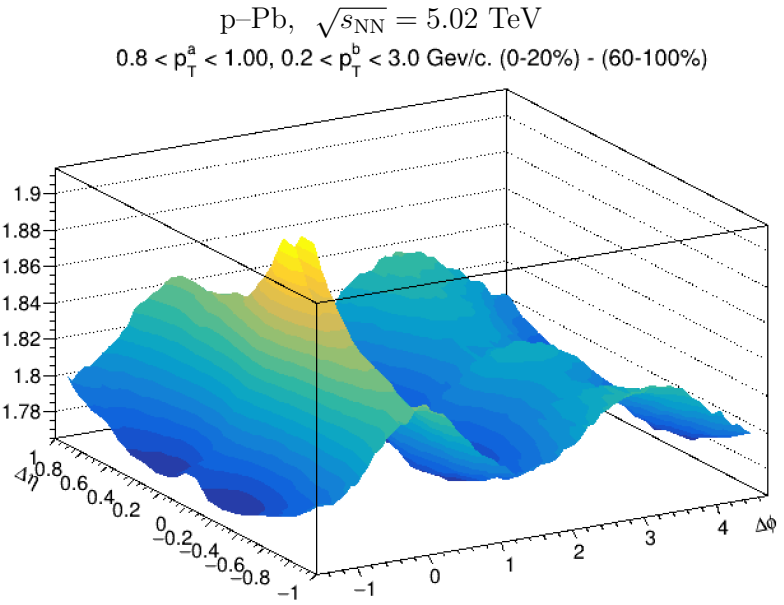

Figure 5.6: Subtracted correlation function [(0–20)% - (60-100)%] for p–Pb collisions at $\sqrt{s_{NN}} = 5.02$ TeV. Zoomed in for clarity. The double ridge structure is more pronounced after subtraction.

b, known as the *baseline* has been inserted, which accounts for the relative difference in multiplicity between central and peripheral collisions, and is defined as the integral along a narrow region surrounding the local minimum located at $\Delta\varphi \approx \pi/2$:

$$b = \int_{-1.6}^{1.6} \int_{\frac{\pi}{2}-0.02}^{\frac{\pi}{2}+0.02} C(\Delta\eta, \Delta\varphi)\ d(\Delta\varphi)d(\Delta\eta). \tag{5.11}$$

Since there is no jet peak located in this region, it is not necessary to include a gap in $\Delta\eta$ (only true when calculating the baseline). A fit produced after a projection onto $\Delta\varphi$ is shown in Fig. 5.7. Calculated χ^2 per the number of degrees of freedom (NDOF) is presented to indicate a satisfactory goodness of fit. $v_2\{2\}(p_{\mathrm{T}})$, $v_2[2](p_{\mathrm{T}})$, and r_2 can then finally be calculated as:

$$\begin{aligned} v_2\{2\}(\mathrm{p_T}\ ) &= \frac{V_{2\Delta}^{\mathrm{a,ref}}}{\sqrt{V_{2\Delta}^{\mathrm{ref,ref}}}} \\ v_2[2](\mathrm{p_T}\ ) &= \sqrt{V_{2\Delta}^{\mathrm{a,a}}} \\ r_2(p_{\mathrm{T}}^{\mathrm{a}}, p_{\mathrm{T}}^{\mathrm{b}}) &= \frac{V_{2\Delta}^{\mathrm{a,b}}}{\sqrt{V_{2\Delta}^{\mathrm{a,a}}\, V_{2\Delta}^{\mathrm{b,b}}}} \end{aligned} \tag{5.12}$$

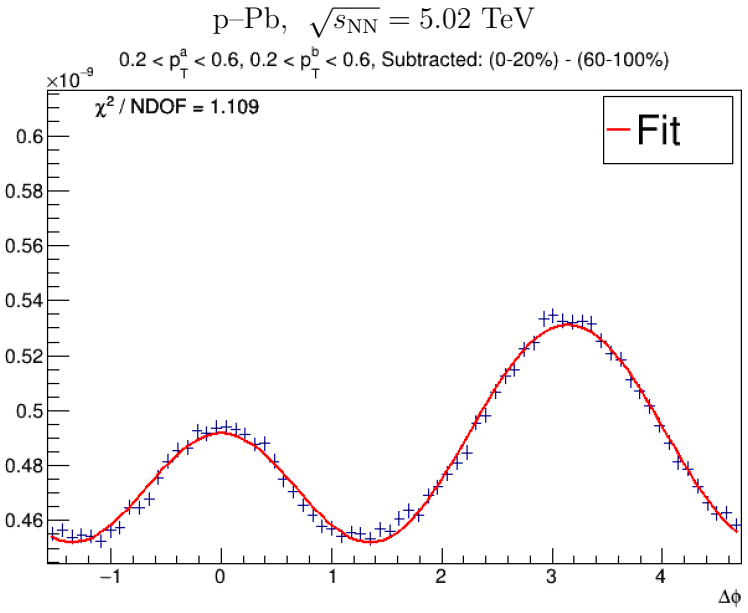

Figure 5.7: Fitted one dimensional correlation function for p–Pb collisions at $\sqrt{s_{\mathrm{NN}}} = 5.02$ TeV and $0.2 < p_T^a < 0.6, 0.2 < p_T^b < 0.6$ GeV/c . A χ^2/ NDOF ≈ 1 indicates that the data is not being overfitted and the fit agrees well with the experimental data.

5.4.2 *Template fit*

The second method in suppressing non-flow is known as the *template fit* method [74]. It relies on the assumption that the one dimensional high multiplicity correlation functions can be approximated as a superposition of low multiplicity correlation functions plus some trigonometric modulation that approximates the double ridge stricture:

$$Y(\Delta\varphi)^{central} = F\, Y(\Delta\varphi)^{peripheral} + G \sum_{n=2}^{3} V_n \cos(\, \Delta\varphi), \tag{5.13}$$

where $Y(\Delta\varphi)^{central}$ and $Y(\Delta\varphi)^{peripheral}$ are the central and peripheral correlation functions, and V_n is the correlator that ultimately produces the desired variables via equation 5.12. In practice, a fit a is performed keeping F, G, and V_n as free parameters. V_2 is then extracted from the fit parameters do obtain the flow observables. Here, a similar assumption is made as in the peripheral subtraction method in that flow is highly suppressed at low multiplicities. Thus, equation 5.13 approximates non-flow with the first term, and flow with the second term. Since $V_{n\Delta}$ is entirely contained in the second term, non flow will be controlled in the final value calculations. However, if there does exist a small amount of flow in the peripheral collisions, then equation 5.13 does not represent a perfect separation between flow and non-flow, and one should expect some residual non-flow in the final values.

Although the above method offers a satisfactory method of controlling non-flow contamination in small systems, it does not account for the observed v_n dependence on multiplicity in p-Pb collisions. Thus, an *improved template fit* method has been implemented by ATLAS in [75], in which the low multiplicity range of 60-100% is broken up into two ranges of 60-80% and 80-100%. The template fit procedure can the be performed twice; once on the outermost collisions (80-100%) relative to the second lowest multiplicity range (60-80%), and then again with the intermediate class of collisions relative to the central most collisions (0-20)%. To limit the number of free parameters, the first fit keeps F

constant and equal to unity:

$$Y(\Delta\varphi)^{intermediate} = Y(\Delta\varphi)^{outer} + G^{intermediate} \sum_{n=2}^{3} V_n{}^{intermediate} \cos(\ \Delta\varphi). \tag{5.14}$$

The second fit includes F as a free parameter (with superscripts now abbreviated for the sake of brevity):

$$Y(\Delta\varphi)^{cent} = F\ Y(\Delta\varphi)^{int} + G^{cent} \sum_{n=2}^{3} V_n{}^{cent} \cos(\ \Delta\varphi). \tag{5.15}$$

The final multiplicty-corrected V_2 can then be extracted as:

$$V_{2\Delta} = V_{2\Delta}^{cent} - \frac{FG^{int}}{G^{cent} + FG^{int}} \times (V_{2\Delta}^{cent} - V_{2\Delta}^{int}). \tag{5.16}$$

Due to the consideration of multiplicity dependence on $V_{2\Delta}$ this thesis focuses on the improved template fit procedure, which will henceforth be abbreviated to *template fit* for the sake of simplicity. However, because the low multiplicity collisions have been separated into two different centrality ranges, the sample sizes in the resulting histograms are smaller, and the number of variables contributing to a final uncertainty value has increased. For this reason, error values associated with the template fit method are by nature larger than the other methods presented above.

5.4.3 *Comparison between template fit and peripheral subtraction*

The results extracted through the template fit method can be compared to the results gathered by using the peripheral subtraction method described in the previous chapter. Before continuing, a striking similarity between the two methods should be noted. Equation 5.9 subtracts a low multiplicity from a high multiplicity histogram, and performs a fit. Now if one were to look at equation 5.13 used for the template fit procedure, it can be seen that by subtracting $F\ Y(\Delta\varphi)^{peripheral}$ from both sides gives the same equation, apart from a factor of F in the low multiplicity correlation function. Thus, it could be argued that the two methods are equivalent up to an additional fit parameter in the

template fit procedure. However, the peripheral subtraction method fits a function to an existing subtracted correlation function. The template fit method fits the sum of a low multiplicity correlation function and a cosine function to the high multiplicity correlation function. This subtle difference could yield a distinct results. Further complicating this is the implementation of multiplicity dependence in the template fit method. Fig. 5.9 and 5.8 shows $v_2[2](p_{\mathrm{T}})$ and $v_2\{2\}(p_{\mathrm{T}})$ for the template fit method and peripheral subtraction method, respectively. The lower panel shows the ratio between the two techniques. It can be observed there is a clear difference in $v_2\{2\}(p_{\mathrm{T}})$ and $v_2[2](p_{\mathrm{T}})$ depending on the method. It can also be observed how the template fit method and calculating $v_2[2](p_{\mathrm{T}})$ give higher statistical uncertainties.

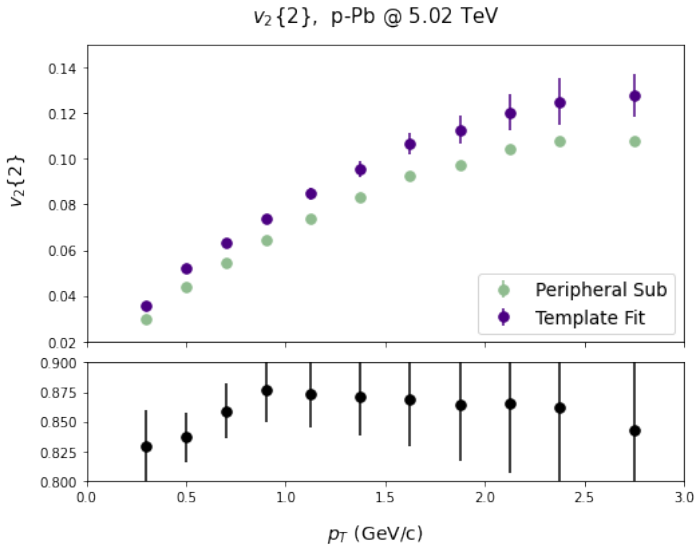

Figure 5.8: Upper panel: $v_2\{2\}(p_{\mathrm{T}})$ calculated by the template fit and peripheral subtraction methods in the (0–20)% centrality range for p–Pb collisions at $\sqrt{s_{\mathrm{NN}}} = 5.02$ TeV. Lower panel: the ratio between the peripheral subtraction and template fit methods for $v_2\{2\}(p_{\mathrm{T}})$.

At low p_{T} , both methods agree to roughly 80%. It can be seen that the ratio between both methods is compatible for $v_2\{2\}(p_{\mathrm{T}})$ and $v_2[2](p_{\mathrm{T}})$. This indicates that value of either observable is influenced by the non-flow suppression techniques in the same way. Now that it has been established that the two non-flow suppression techniques yield different results, $\frac{v_2\{2\}(p_{\mathrm{T}})}{v_2[2](p_{\mathrm{T}})}$ for each method can now be compared. Fig. 5.10 shows $\frac{v_2\{2\}(p_{\mathrm{T}})}{v_2[2](p_{\mathrm{T}})}$ measured using periheral subtraction

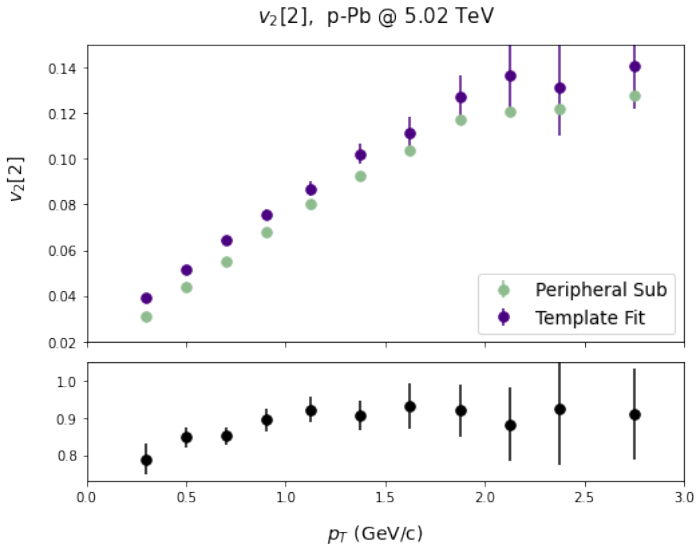

Figure 5.9: Upper panel: $v_2[2](p_{\mathrm{T}})$ calculated by the template fit and peripheral subtraction methodsin the (0–20)% centrality range for p–Pb collisions at $\sqrt{s_{\mathrm{NN}}} = 5.02$ TeV. Lower panel: the ratio between the peripheral subtraction and template fit methods for $v_2[2](p_{\mathrm{T}})$.

and the template fit method. The results do not appear to be compatible. The peripheral subtraction method does not contain the jump between the first two p_{T} bins that is seen in the template fit method. In most p_{T} bins, the template fit method measures a smaller deviation from unity in comparison to peripheral subtraction. The results to not appear to be compatible, although they do show a qualitatively similar trend beyond the first p_{T} bin. Again, systematic errors are very large and dominate the experimental uncertainty, even more so in the peripheral subtraction technique. The reason for this is likely the same reason as described in section 5.6.1.

Now, one can also compare r_2 and see if the two methods are in agreement. Fig. 5.11 shows r_2 calculated by template fit and peripheral subtraction. A far greater degree of agreement is seen in contrast to what was observed in $\frac{v_n\{2\}(p_{\mathrm{T}})}{v_n[2](p_{\mathrm{T}})}$. This could be because the subtraction methods are more similar when considering correlation functions from a narrower p_{T} range.

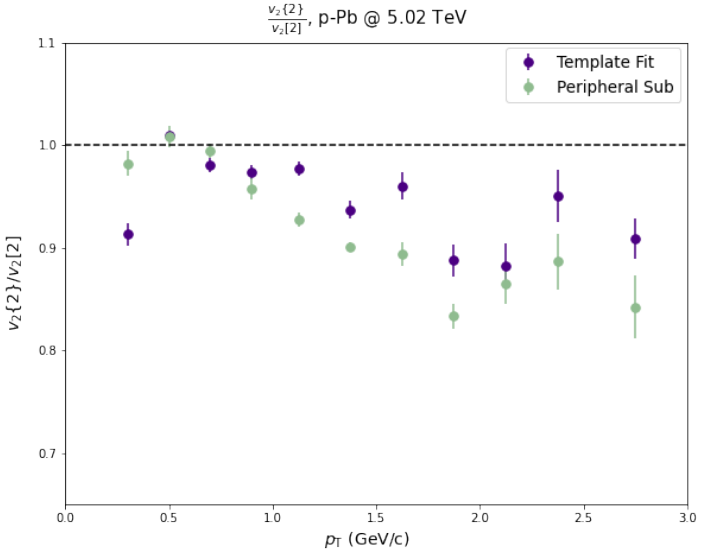

Figure 5.10: New measurement of $\frac{v_2\{2\}(p_T)}{v_2[2](p_T)}$ calculated by peripheral subtraction and template fit methods in the (0–20)% centrality range for p–Pb collisions at $\sqrt{s_{NN}} = 5.02$ TeV.

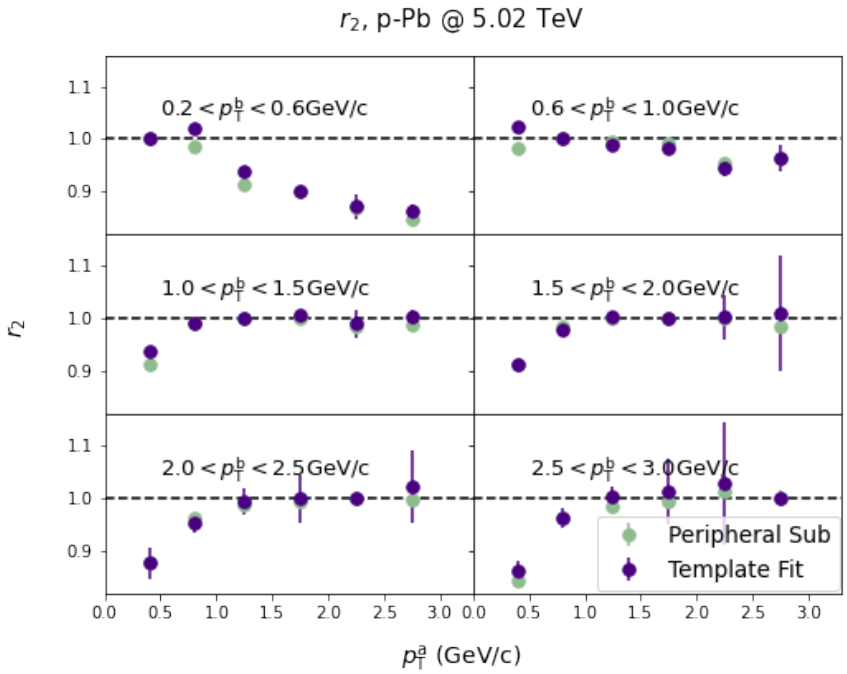

Figure 5.11: New Measurement of r_2 by peripheral subtraction and template fit methods in the (0–20)% centrality range for p–Pb collisions at $\sqrt{s_{NN}} = 5.02$ TeV.

Fig. 5.11 shows that the two analysis methods in this thesis are compatible when calculating r_2, yet it has been seen they are not as compatible with $\frac{v_2\{2\}(p_T)}{v_2[2](p_T)}$.

5.4.4 *Estimation of remaining non-flow*

Now, the efficacy of the non-flow suppression techniques can be explored. First, a plot showing $V_2^{a,ref}$ prior to any non-flow suppression is shown in Fig. 5.12. Here, ALICE data is superimposed with Monte Carlo simulation data from DPMJET [40]. It can be seen that $V_2^{a,ref}$ calculated from DPMJET is far greater than ALICE data. This is because of the jet contributions and non-flow processes that introduce significant anisotropy into the system, although these processes can not be described as collective effects.

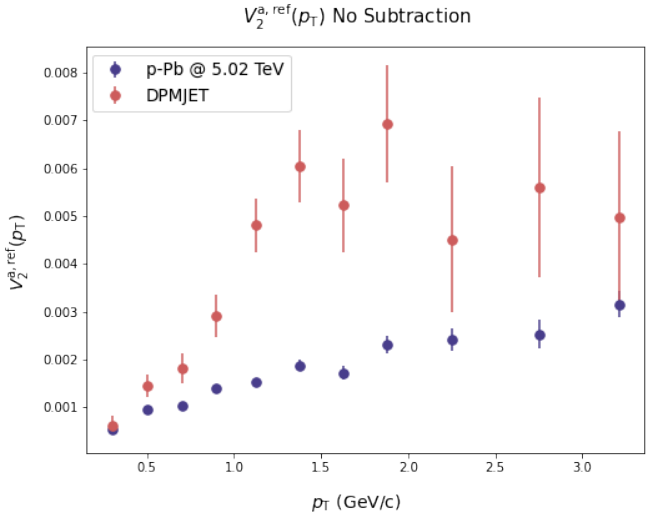

Figure 5.12: $V_2^{a,ref}$ prior to non-flow suppression from ALICE and DPMJET simulation in the (0–20)% centrality range for p–Pb collisions at $\sqrt{s_{NN}} = 5.02$ TeV.

Since DPMJET only includes non-flow processes, it is expected that after a non-flow suppression procedure its signal in V_2 should be greatly reduced. This section deals directly with instead of v_2, since the presence of square roots and fractions in the definitions of $v_2\{2\}(p_T)$ and $v_2[2](p_T)$ would not be able to handle the small and negative numbers that will be encountered. Fig. 5.13 a and b shows $V_n^{a,a}$ for peripheral subtraction and template fit, respectively. Also

shown is DPMJET data, which is then then fit to a zero degree polynomial shown in grey, whose fit parameter is denoted with 'remaining non-flow'. In both

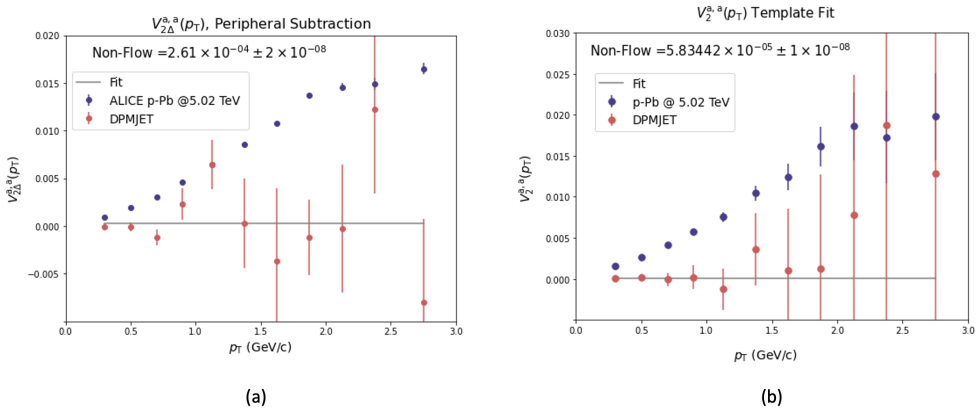

Figure 5.13: $V_2^{\mathrm{a,a}}$ after non-flow suppression from ALICE data and DPMJET simulation in the (0–20)% centrality range for p–Pb collisions at $\sqrt{s_{\mathrm{NN}}} = 5.02$ TeV. **(a):** peripheral subtraction. **(b):** template fit.

methods, the non-flow suppression procedure has worked fairly well for low-p_{T} . In peripheral subtraction, as p_{T} increases, the DPMJET simulation begins to fluctuate around zero. In template fit, the DPMJET simulation begins to deviate from p_{T} , although it appears to increase instead of fluctuate. However, in both methods the statistical uncertainty becomes so large after roughly 1 GeV/c that it is hard to determine how much non-flow is remaining. The estimation of remaining non-flow derived from the fit appears to be smaller in the template fit by an order of magnitude. However, since the statistical uncertainty is so large, and there appears to be the potential for p_{T} dependence in DPMJET data in the case of template fit, no hard conclusions should be drawn from the fit parameters. The large magnitude of DPMJET measurements that are starting to become apparent at $p_{\mathrm{T}} = 2.75$ is the reason why this analysis was truncated at 3.0 GeV/c. Beyond this value, a case can be made that non-flow is still present, particularly in $V_n^{\mathrm{a,a}}$.

The same study from $V_n^{\mathrm{a,ref}}$ yields different results. Fig. 5.14 shows an identical analysis performed for $V_n^{\mathrm{a,ref}}$. Here, the DPMJET data has much smaller statistical uncertainty and no p_{T} dependence is observed. As was the case in Fig. 5.13, the fit resulting from template fit method differs from the peripheral subtraction method by roughly an order of magnitude. This could suggest

that the template fit method is more effective than the peripheral subtraction method in suppressing non-flow.

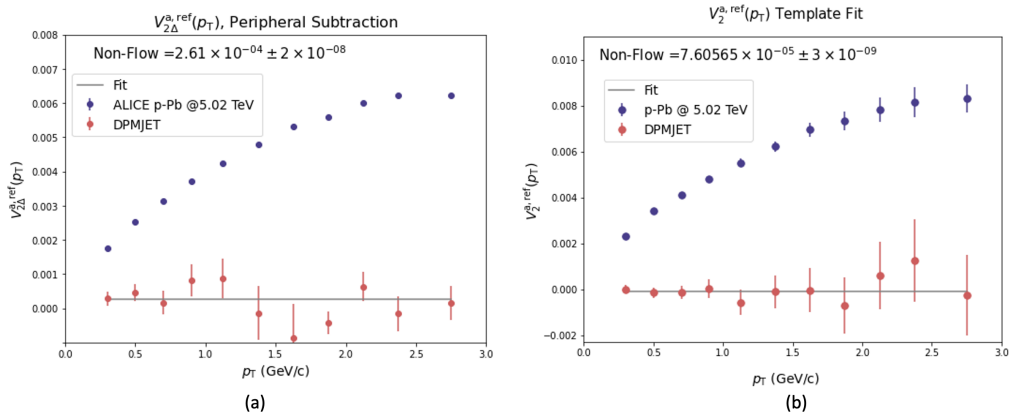

Figure 5.14: $V_2^{\mathrm{a,ref}}$ after non-flow suppression from ALICE data and DPMJET simulation in the (0–20)% centrality range for p–Pb collisions at $\sqrt{s_{\mathrm{NN}}} = 5.02$ TeV. **(a):** peripheral subtraction. **(b):** template fit.

Lastly, $V_2^{\mathrm{a,b}}$ is analyzed. Fig. 5.15 displays $V_2^{\mathrm{a,b}}$ for both ALICE data and DPMJET simulation. In the template fit method, larger statistical uncertainties are observed, although both methods fluctuate around the fit line. A noticeably different characteristic of Fig. 5.15 is the difference in fit parameter value between peripheral subtraction and template fit. In the previous examples, the template fit method had a smaller fit parameter value by roughly an order of magnitude. Here, however, for most cases of $^{\mathrm{a}}_{\mathrm{T}}$ the situation is the opposite: the fit parameter from the peripheral subtraction technique is smaller by roughly an order of magnitude in comparison to template fit. This could possibly point towards a reason for the relative agreement between the two non-flow suppression techniques in r_2 , and the difference in $\frac{v_2\{2\}(p_{\mathrm{T}})}{v_2[2](p_{\mathrm{T}})}$.

It has been shown that in $V_2^{\mathrm{a,ref}}$ and $V_2^{\mathrm{a,a}}$ specifically, the peripheral subtraction and template fit could be suppressing non-flow by different amounts. This could account for the difference between the two methods observed in $\frac{v_2\{2\}(p_{\mathrm{T}})}{v_2[2](p_{\mathrm{T}})}$.

However, it was also seen that there is an opposite effect in non-flow in $V_2^{\mathrm{a,b}}$, which would suggest that r_2 should also differ in relation to template fit and peripheral sub. Further study would be required to support the hypothesis that each non-flow technique affects non-flow differently.

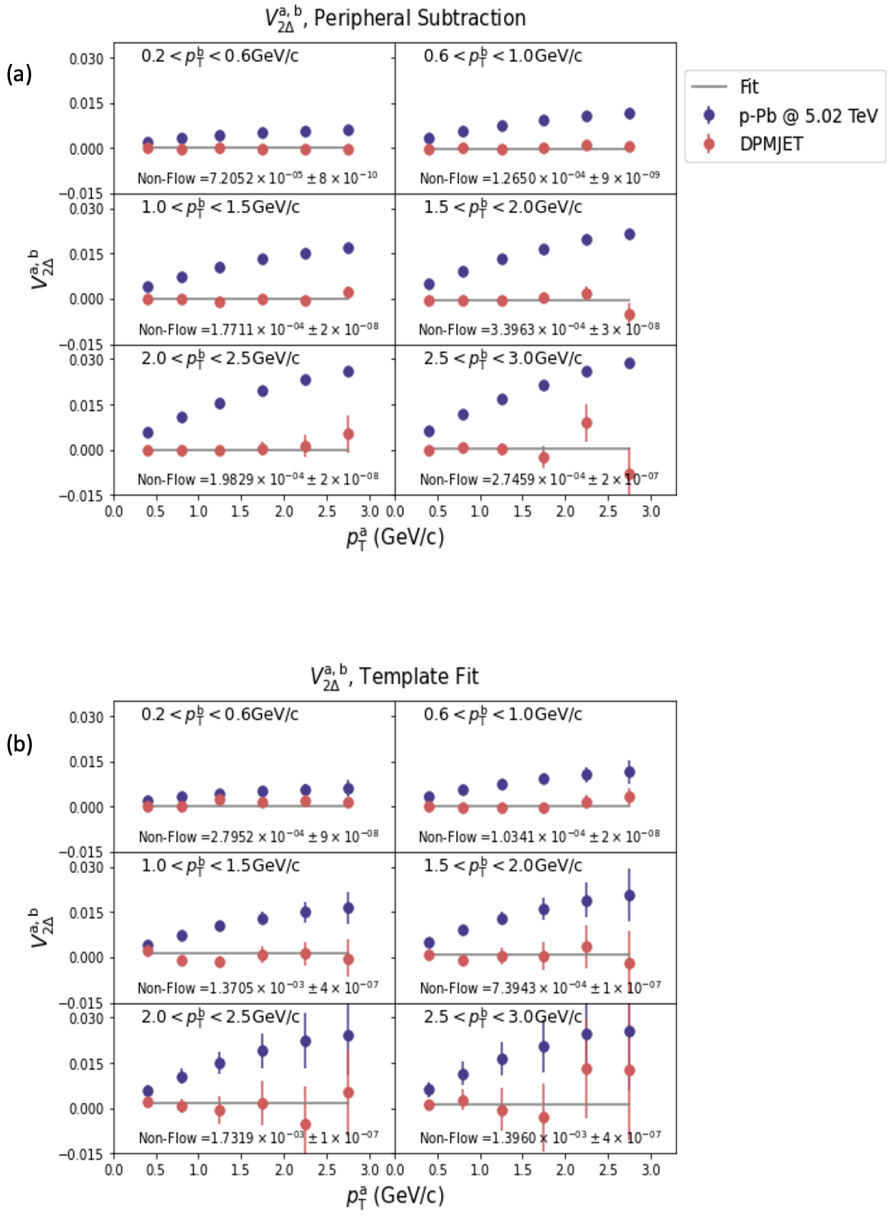

Figure 5.15: $V_2^{a,b}$ after non-flow suppression from ALICE p–Pb collisions at $\sqrt{s_{NN}}$ 5.02 TeV, and DPMJET simulation. **(a):** peripheral subtraction. **(b):** template fit.

5.5 Systematic examples

Examples of the systematic study performed will now be discussed, and the remainder are contained in appendix B. The event selection cut of the primary

vertex, PV_z is shown below for $\frac{v_2\{2\}(p_T)}{v_2[2](p_T)}$ and r_2 in both the template fit method and ther peripheral subtraction method. Fig. 5.16 (a) shows the ratio between default and variational cuts for $\frac{v_2\{2\}(p_T)}{v_2[2](p_T)}$ in the upper panel for the peripheral subtraction method. The lower panel shows value of the Barlow test. Fig. 5.16 (b) shows the same calculations, but for the template fit method. A zero degree fit is also shown in the upper panels, which is what is used to assign systematic error by subtracting the value of the fit from unity if the average of the barlow test over p_T is greater than 2. It is seen that neither method passes the Barlow test, and neither measurement contributed to the systematic error. A point of interest is the 'jump' seen at $p_T = 0.5$ GeV/c in template fit. This is present for the both event and track variations, although not for variations in $|\Delta\eta|$. This suggests that the event cuts chosen in the default analysis have some influence in the single-particle p_T distributions, resulting in a non trivial fluctuation in that specific point. A table showing the average Barlow calculated in $\frac{v_2\{2\}(p_T)}{v_2[2](p_T)}$

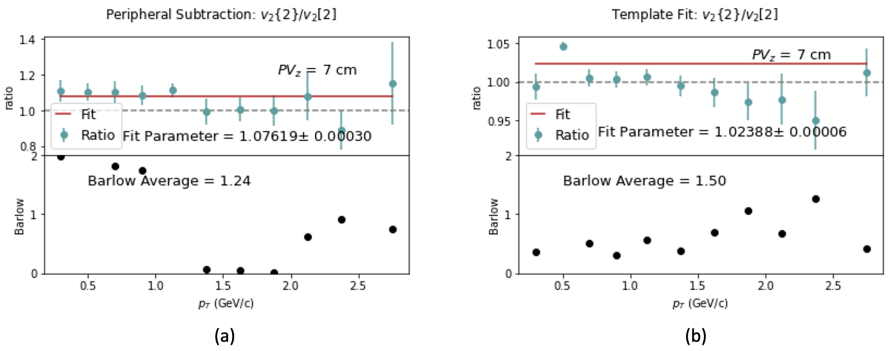

Figure 5.16: Systematic study in the variation of primary vertex in **(a):** peripheral subtraction, and **(b):** template fit.

is now shown in table 5.1. For both the peripheral subtraction and template fit method, none of the systematic variations pass the Barlow test. An interesting source of systematic error that was not analyzed was changing the centrality ranges used in peripheral subtraction and template fit. For example, in the peripheral subtraction technique, low multiplicity of 70-100% could have been checked. This would have been useful in demonstrating the stability of the results and should be used in all future analyses.Similar tables are provided for r_2 in template fit and peripheral subtraction are provided in tables 5.2 and 5.3, respectively. Here, Barlow averages are reported individually for values of p_T^b,

and it is seen that some p_{T} intervals begin to pass the Barlow test. If there is a pass, then a fit is performed and subtracted from unity to apply a systematic uncertainty. This results in significantly larger systematic errors in peripheral subtraction than in template fit.

Barlow Average, $\frac{v_2\{2\}(p_{\mathrm{T}})}{v_2[2](p_{\mathrm{T}})}$		
Systematic Variation	Template Fit	Peripheral Subtraction
Primary Vertex	1.49	1.24
$\lvert\Delta\eta\rvert > 1$	1.94	1.39
$\lvert\Delta\eta\rvert > 2$	1.23	1.33
Filterbit	1.50	1.23
# TPC Cl.	1.07	0.93
χ^2/TPC Cl.	1.19	0.08

Table 5.1: Barlow average pertaining to the systematic variations in $\frac{v_2\{2\}(p_{\mathrm{T}})}{v_2[2](p_{\mathrm{T}})}$ for template fit and peripheral subtraction. No sources of systematic uncertainty pass the Barlow test and thus will not be considered in the final systematic uncertainty.

Barlow Average, Template Fit						
	$p_{\mathrm{T}}^{\mathrm{b}}$ (GeV/c)					
Systematic Variation	$0.2 < p_{\mathrm{T}}^{\mathrm{b}} < 0.6$	$0.6 < p_{\mathrm{T}}^{\mathrm{b}} < 1.0$	$1.0 < p_{\mathrm{T}}^{\mathrm{b}} < 1.5$	$1.5 < p_{\mathrm{T}}^{\mathrm{b}} < 2.0$	$2.0 < p_{\mathrm{T}}^{\mathrm{b}} < 2.5$	$2.5 < p_{\mathrm{T}}^{\mathrm{b}} < 3.0$
Primary Vertex	3.17	1.97	1.00	2.14	0.83	1.61
$\lvert\Delta\eta\rvert > 1$	0.91	0.88	0.59	0.32	0.11	0.33
$\lvert\Delta\eta\rvert > 2$	1.09	1.16	0.55	0.42	0.17	0.51
Filterbit	3.50	1.23	0.74	2.44	0.81	1.4
# TPC Cl.	3.23	1.71	0.75	2.28	0.84	1.35
χ^2/TPC Cl.	0.00	1.23	0.70	1.31	0.45	1.30

Table 5.2: Barlow average pertaining to the systematic variations in r_2 for template fit. Sources that pass the minimum Barlow average requirements are highlighted in green, and are used in determining final systematic uncertainty.

Barlow Average, Peripheral Subtraction						
	$p_{\mathrm{T}}^{\mathrm{b}}$ (GeV/c)					
Systematic Variation	$0.2 < p_{\mathrm{T}}^{\mathrm{b}} < 0.6$	$0.6 < p_{\mathrm{T}}^{\mathrm{b}} < 1.0$	$1.0 < p_{\mathrm{T}}^{\mathrm{b}} < 1.5$	$1.5 < p_{\mathrm{T}}^{\mathrm{b}} < 2.0$	$2.0 < p_{\mathrm{T}}^{\mathrm{b}} < 2.5$	$2.5 < p_{\mathrm{T}}^{\mathrm{b}} < 3.0$
Primary Vertex	6.08	1.49	2.66	2.76	2.66	3.21
$\lvert\Delta\eta\rvert > 1$	3.12	1.50	2.11	2.74	2.79	2.81
$\lvert\Delta\eta\rvert > 2$	0.84	1.28	1.91	2.08	2.21	2.17
Filterbit	6.64	1.47	2.40	2.97	2.77	3.02
# TPC Cl.	6.90	1.18	2.55	3.17	2.62	3.03
χ^2/TPC Cl.	6.66	1.24	2.47	3.21	2.67	3.07

Table 5.3: Barlow average pertaining to the systematic variations in r_2 for peripheral subtraction. Sources that pass the minimum Barlow average requirements are highlighted in green, and are used in determining final systematic uncertainty.

5.6 Results and discussion

In large systems anisotropic flow and jet-quenching measurements, among others, provide strong evidence supporting the hypothesis that the quark gluon plasma is created in high energy collisions. A common signal that is observed in particular is the double ridge structure in two particle correlation functions, which can be explained by the creation and evolution of the QGP. Recent analyses (including this thesis) in high multiplicity collisions in small systems have shown that a similar double ridge structure is also observed, one of these systems being the p–Pb collisions studied in this work. This raises the critical question: is the source of the collective phenomena observed in small systems the same as the collective phenomena observed in large systems? If yes, then one could be able to conclude that the QGP is created in systems which fundamental theory does not predict is possible. In other words, evidence from small system collisions motivate us to ask if modern high energy physics experiments are capable of creating the smallest droplet of QGP.

Further measurements are required in order to determine the origin of flow-like phenomena in small systems. Ultimately, these measurements must then be compared to theoretical models that attempt to describe the data. The model which describes the data the best will represent the best understanding of the collision dynamics. This thesis measures flow vector fluctuations in p–Pb systems in order to provide constraints for future models aiming to describe collectivity and flow in small systems. For both r_2 and $\frac{v_2\{2\}(p_\mathrm{T})}{v_2[2](p_\mathrm{T})}$, theoretical modelling is not currently available, and to make claims about the origin of the observed flow vector fluctuations, comparison to theoretical modelling is needed. Such assertions can be made at a later time when modelling for these particular observables is available.

Now, final results are reported for $\frac{v_2\{2\}(p_\mathrm{T})}{v_2[2](p_\mathrm{T})}$ and r_2 , and physics conclusions can be drawn. It has been shown that both methods have successfully removed a significant amount of non-flow, which implies that the remaining data is dominated by collective flow. This improves upon the previous measurement in p–Pb collisions in [27], where non-flow significantly affected the data. Moreover, these measurements can constrain speculation over the origin of a flow signal in small

systems, as theoretical modelling should also be able to reproduce the results shown below in r_2 and $\frac{v_2\{2\}(p_T)}{v_2[2](p_T)}$.

5.6.1 $\frac{v_2\{2\}(p_T)}{v_2[2](p_T)}$ *results*

In the study of $\frac{v_2\{2\}(p_T)}{v_2[2](p_T)}$, it is instructive to first look at $v_2\{2\}(p_T)$ and $v_2[2](p_T)$ individually. Measured $v_2\{2\}(p_T)$ and $v_2[2](p_T)$ as calculated by the template fit method in 0-20% centrality collisions at $\sqrt{s_{NN}} = 5.02$ TeV are now presented in Fig. 5.17. While at low p_T , the values of $v_2[2](p_T)$ and $v_2\{2\}(p_T)$ can be seen to be in agreement with one another, a deviation can be seen with increasing p_T , already showing the affect of flow-vector fluctuations in $v_2\{2\}(p_T)$. It can also be seen that the uncertainties in $v_2[2](p_T)$ are notably larger than that of $v_2\{2\}(p_T)$. This is because $v_2[2](p_T)$ requires the selection of two particles from the same narrow range in p_T . After suppressing non-flow to almost zero, a significant flow signal is still observed and is similar to the signal seen in Pb–Pb [76, 77]. The most central collisions have a minimum degree of spatial anisotropy, causing a smaller value of v_2, and v_2 is mostly driven by fluctuations in the initial state. As collisions become more peripheral, spatial anisotropy increases, and there is a marked increase in v_2. Measurements of $v_2\{2\}(p_T)$ in similar centralities between Pb–Pb collisions and non-flow suppressed p–Pb collisions are qualitatively in agreement. This suggests that the same source of flow in Pb–Pb collisions could possibly be present in p–Pb.

Now, the ratio between $\frac{v_2\{2\}(p_T)}{v_2[2](p_T)}$ and $v_2[2](p_T)$ can be taken to yield $\frac{v_2\{2\}(p_T)}{v_2[2](p_T)}$. A deviation from unity is observed, indicating the presence of p_T dependent flow vector fluctuations. Fig. 5.18 shows $\frac{v_2\{2\}(p_T)}{v_2[2](p_T)}$ measured by the template fit and peripheral subtraction methods. A deviation from unity is observed with p_T in both methods. No systematic uncertainties contribute to the final uncertainties. Although both methods are display similar p_T dependent trends, there the template fit yields a higher value of $\frac{v_2\{2\}(p_T)}{v_2[2](p_T)}$ beyond the unit of one standard deviation for most p_T intervals. This could be the result of the two suppression methods treating various sources of non-flow differently, leading to a different measurement.

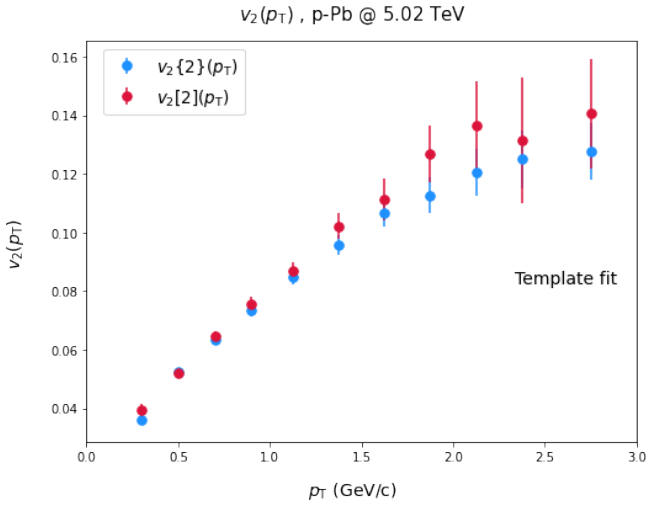

Figure 5.17: $v_2\{2\}(p_{\mathrm{T}})$ and $v_2[2](p_{\mathrm{T}})$ in 0–20% centrality collisions at $\sqrt{s_{\mathrm{NN}}} =$ 5.02 TeV using the template fit method. Disagreement between the two methods begin to manifest as p_{T} increases.

A point of particular interest is the relatively low value in the first p_{T} bin of the template fit method, which jumps sharply into the next p_{T} bin. Interestingly, hydrodynamic calculations have shown strong deviations below unity at low p_{T} in Pb–Pb collisions [78]. However, it is not clear whether this same trend would be reproduced in p–Pb collisions, and a direct comparison to these models is not possible. The 'jump' also disappears by taking a smaller $\Delta\eta$ range, which yields higher statistics. This could mean that given higher statistics, the trend could become more smooth. However, in order to ensure that the jet peak is entirely eliminated, results with smaller $\Delta\eta$ gaps are not reported. In systematic checks, it is noted that the first p_{T} point is relatively stable for event and track cut variations. Both methods provide constraints on the origin of a flow signal in small systems, since they both predict a breakdown of factorization that depend on p_{T} , with a magnitude of $\frac{v_2\{2\}(p_{\mathrm{T}})}{v_2[2](p_{\mathrm{T}})}$ of roughly 0.9 at 2.75 GeV/c. Although the values differ from [27], a similar deviation from unity is observed in 0-20% centrality collisions. Fig. 5.19 shows the previous ALICE measurement of $\frac{v_2\{2\}(p_{\mathrm{T}})}{v_2[2](p_{\mathrm{T}})}$. While the previously published results and the current results show a deviation from unity, the new results are of higher quality, since non-flow has been greatly diminished. The produced signal, therefore, is the result 'flow-like' effects. Moreover, the current analysis measures the

presence of flow vector fluctuations at much lower values of p_{T} . These new measurements also provide a finer p_{T} resolution than the previous study. In a comparison of the data to a theoretical model, one could tune the parameters of the medium such as η/s, and compare to the results measured in large systems to see if the parameters are the same. Similar values of η/s could indicate a similar medium has been created between large and small systems. Moreover, finer p_{T} resolution gives more points of comparison to models and thus a more sophisticated and detailed comparison can be made.

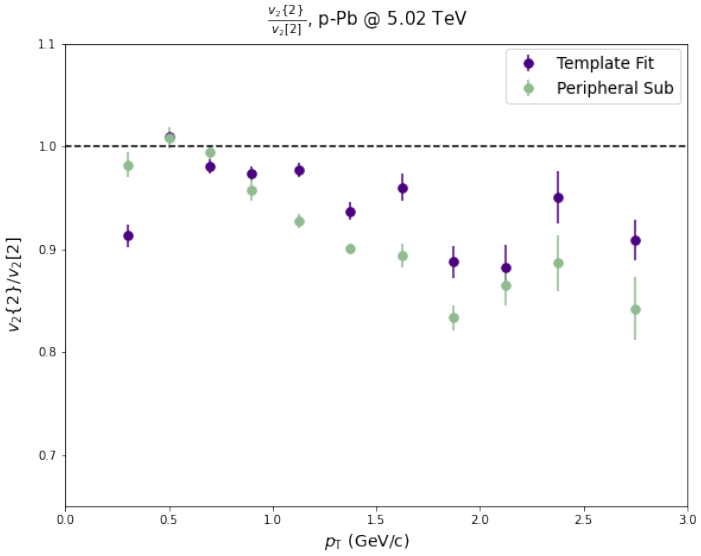

Figure 5.18: $\frac{v_2\{2\}(p_{\mathrm{T}})}{v_2[2](p_{\mathrm{T}})}$ in 0–20% centrality collisions at $\sqrt{s_{\mathrm{NN}}}$ = 5.02 TeV calculated by the template fit and peripheral subtraction method. Deviation from unity is observed as a function of p_{T} .

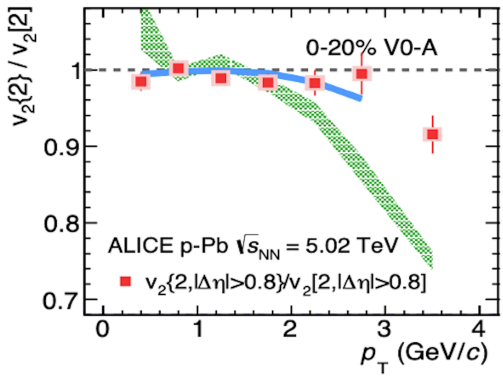

Figure 5.19: Measured $\frac{v_2\{2\}(p_T)}{v_2[2](p_T)}$ in p–Pb 0-20% centrality collisions at $\sqrt{s_{NN}}$ measured by ALICE in 2017 [27]. Also shown is model comparisons to MUSIC in the blue line, and DPMJET in the green shaded region.

5.6.2 r_2 *results*

Since r_2 calculates correlations from many different p_T intervals, it provides much more detailed information about factorization and the correlation structure in comparison to $\frac{v_2\{2\}(p_T)}{v_2[2](p_T)}$. This is a valuable advantage when comparing to a theoretical model, as a greater number of data points allows for a more detailed and sensitive comparison. Measurements of r_2 are now reported below in Fig. 5.20. These results will also be compared to the previous measurement in p–Pb by ALICE, and also a similar study performed by CMS [79]. Again, a deviation from unity is observed, this time for all p_T^b, implying a breakdown in factorization. Theoretical models hoping to describe high energy p–Pb data must be able to reproduce this breakdown of factorization for all p_T intervals, providing an important constraint on future models. Moreover, the two methods of template fit and peripheral subtraction display a high degree of agreement in r_2 . This could be because the non-flow suppression techniques give a more similar treatment of non-flow when the p_T intervals are smaller. Regardless of the origin, r_2 provides a much more stringent constraint on future theoretical modelling, since there is little variation between the two methods. As expected, statistical uncertainties are higher in r_2 in comparison to $\frac{v_2\{2\}(p_T)}{v_2[2](p_T)}$, particularly in the highest p_T ranges, where the sample sizes are the smallest. A large systematic error is reported in the lowest p_T^a bin for both methods, although the peripheral subtraction technique contains higher systematic uncertainties

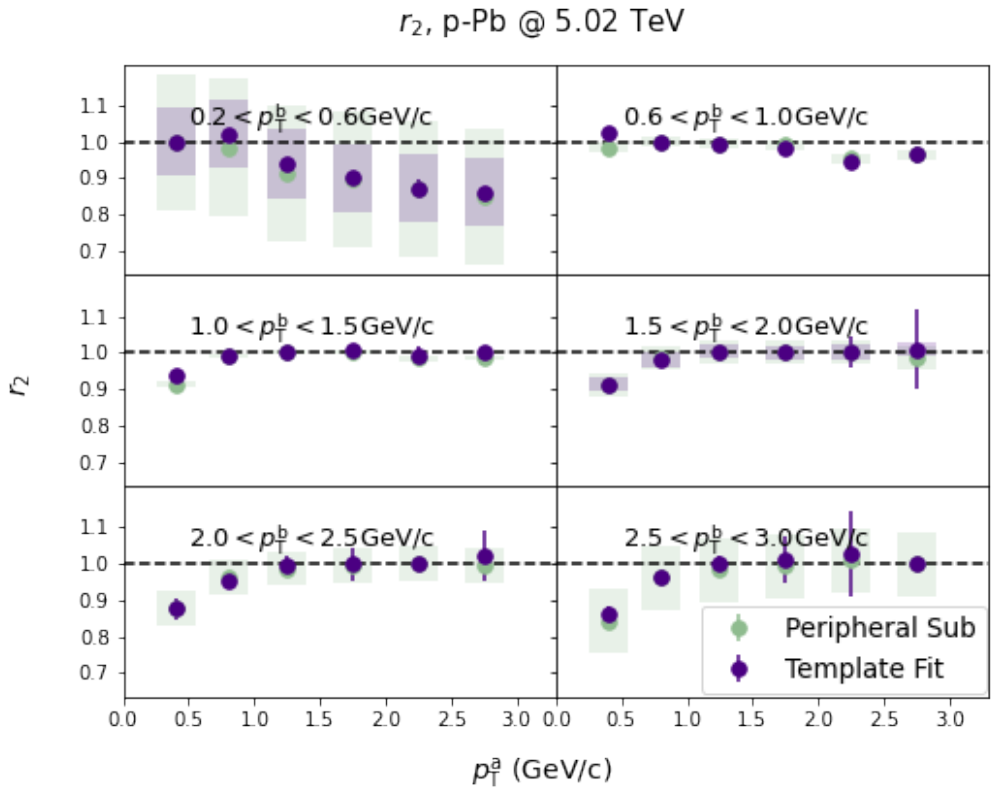

Figure 5.20: r_2 calculated by the template fit and peripheral subtraction method. Deviation from unity is observed for $p_{\mathrm{T}}^{\mathrm{a}}$ ranges. Note that r_2 is by construction symmetric (i.e $r_2(p_{\mathrm{T}}^{\mathrm{a}}, p_{\mathrm{T}}^{\mathrm{b}}) = r_2(p_{\mathrm{T}}^{\mathrm{b}}, p_{\mathrm{T}}^{\mathrm{a}})$). Shaded bars indicate systematic error. When $p_{\mathrm{T}}^{\mathrm{a}} = p_{\mathrm{T}}^{\mathrm{b}}$, $r_n = 1$, forcing the statistical uncertainties to be zero through the bootstrap procedure.

in all p_{T} intervals. A large number of particles produced are within the range of $0.2 < p_{\mathrm{T}} < 0.6$, meaning that in the upper left panel of Fig. 5.20, $p_{\mathrm{T}}^{\mathrm{b}}$ acts as an approximation to the reference flow. Thus, it is expected that this panel should reasonably well approximate the results from $\frac{v_2\{2\}(p_{\mathrm{T}})}{v_2[2](p_{\mathrm{T}})}$. Within systematic errors, an agreement is observed between Fig. 5.20 and Fig. 5.18.

Now the measured values of r_2 can be compared to the previous studies from ALICE and CMS, however both of the previous studies contain no non-flow suppression techniques and claim significant non-flow contamination. First, the current results are shown next to the previous ALICE study in p–Pb collisions at $\sqrt{s_{\mathrm{NN}}} = 5.02$ TeV for various collision centralities in Fig. 5.21. The 0-20% centrality offers a comparison to this study, but it is interesting to note

that deviations from unity are recorded in the higher centrality ranges where the double ridge is not observed. This is likely due to the presence of non-flow contamination which can be confirmed by a number of points laying significantly above one. Since r_n is constrained to be less than or equal to one by the Cauchy-Schwartz inequality, this is an indication that non-flow is contaminating the data in the higher centrality ranges. In the 0-20% centrality ranges, however, the new study reports a slightly larger deviation from unity than the previous ALICE measurement with no non-flow suppression. Again, this measurement provides more reliable clues into the origin of a flow signal in small systems since it effectively eliminates non-flow.

The measurements from this thesis can also be compared to a similar CMS study in p–Pb collisions [79] (which was also performed on run-1 data), although a comparison to similar centrality ranges becomes difficult, since the CMS collaboration uses different centrality estimation techniques. Fig. 5.22 shows a comparison between CMS measurements of r_2 in p–Pb collisions at $\sqrt{s_{\mathrm{NN}}} = 5.02$ TeV and the measurements in 0-20% centrality from this thesis. Again, similar trends are noted between the results produced in this work and previous measurements, specifically a decrease in factorization ratio with $|p_{\mathrm{T}}^{\mathrm{a}} - p_{\mathrm{T}}^{\mathrm{b}}|$. Fluctuations above one are present in the lower multiplicity region measurements produced by CMS, implying the presence of non-flow contamination. Again, the results produced in this work are an improvement on the previous measurement to the suppression of non-flow, and higher sample sizes in comparison to the previous run-1 data.

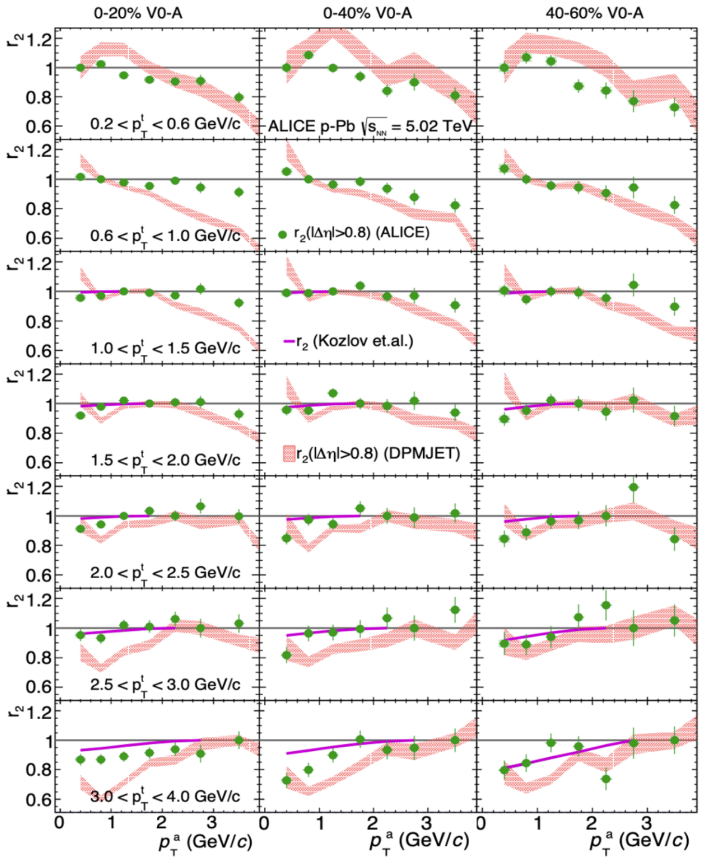

Figure 5.21: Previously measured r_2 from ALICE [27] in various centralities for p–Pb collisions at $\sqrt{s_{\mathrm{NN}}} = 5.02$ TeV. The magenta line represents hydrodynamic calculations (MUSIC) with MC-Glauber initial conditions. The red shaded region represent Monte Carlo DPMJET calculations that contain no hydrodynamics.

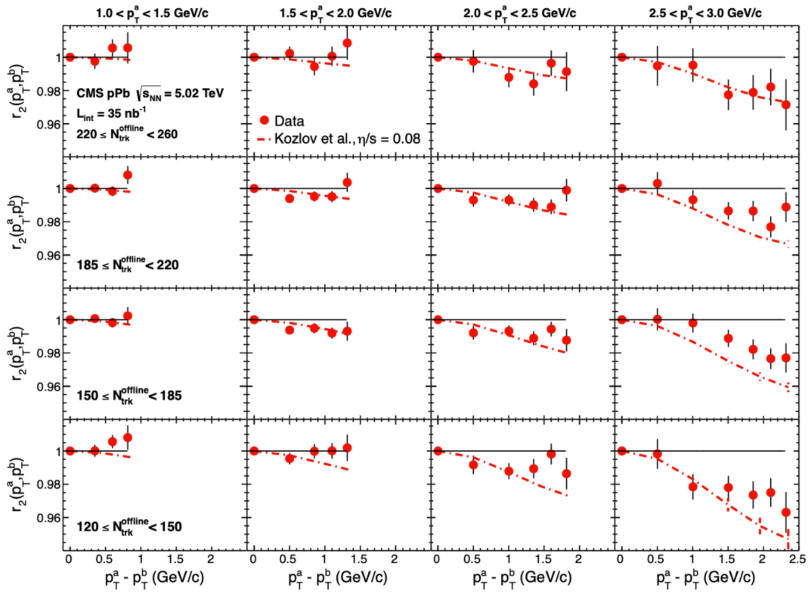

Figure 5.22: Previously measured r_2 from CMS [79] in various centralities (denoted by $N_{\mathrm{trk}}^{\mathrm{offline}}$) for p–Pb collisions at $\sqrt{s_{\mathrm{NN}}} = 5.02$ TeV. Here, the results are presented in terms of $p_{\mathrm{T}}^{\mathrm{a}} - p_{\mathrm{T}}^{\mathrm{b}}$. The red line represents hydrodynamic calculations [80] with modified MC-Glauber initial conditions.

Chapter 6

Conclusion

A flow signal in p–Pb collisions has been observed similar to that seen in Pb–Pb collisions. Moreover, a double ridge structure in high multiplicity two particle correlation functions has also been observed in p–Pb collisions. In Pb–Pb collisions, these signatures are thought to be the result of the dynamically expanding quark gluon plasma medium. The compelling similarities between measurements in small and large systems has lead to speculation that the same underlying processes could be present in both systems, which is entirely unexpected. Hence, investigations into the origins of flow and collectivity in small systems must be performed in order to gain better theoretical understanding of the observed phenomena.

This thesis presented an analysis of flow-vector fluctuations in high multiplicity p–Pb collisions at $\sqrt{s_{\mathrm{NN}}} = 5.02$ TeV. A practical issue concerning such measurements is the presence of non-flow, which is dominant in small systems and must be suppressed when conducting flow analyses. Here, two different methods of non-flow suppression were applied in order to procure more robust measurements of r_2 and $\frac{v_2\{2\}(p_{\mathrm{T}})}{v_2[2](p_{\mathrm{T}})}$ than the previous studies in ALICE [27] and CMS [79], where non-flow contamination in p–Pb collisions as significant. The two methods of non-flow suppression (peripheral subtraction and template fit) were then compared and their effectiveness was explored using DPMJET simulation. At transverse momenta below 3 GeV/c, evaluations of DPMJET simulation indicate non-flow has been significantly reduced after the peripheral subtraction and template fit procedures.

The main results of this work are measurements of $\frac{v_2\{2\}(p_\mathrm{T})}{v_2[2](p_\mathrm{T})}$ and r_2 using the discussed non-flow suppression techniques, which included a systematic study of event and track selection variations. These results show a clear deviation from unity across both observables and suppression methods, which indicates the presence of p_T dependent flow vector fluctuations. Furthermore, while a strong conformity between the two methods is present in r_2 , $\frac{v_2\{2\}(p_\mathrm{T})}{v_2[2](p_\mathrm{T})}$ measurements are not in quantitative agreement. These measurements provide constraints on future theoretical models aiming to describe anisotropic flow and collectivity in small systems. Thus, the measurements performed in this work can help interpret flow and collectivity in small systems and constrain speculation over its origins.

Future work is required to determine the source of variance seen in the measurements of $\frac{v_2\{2\}(p_\mathrm{T})}{v_2[2](p_\mathrm{T})}$ using template fit and peripheral subtraction. Furthermore, an explanation as to why this variance is not seen in r_2 measurements is also needed. In evaluating the efficacy of the non-flow suppression methods, non-flow modelling with smaller statistical uncertainty would also be a useful tool, as perhaps with smaller uncertainties it can be shown that non-flow remains negligible beyond 3 GeV/c, thus extending the p_T reange of this analysis. Additionally, a more extensive systematic study is required in order make the analysis more comprehensive. Lastly, to make available more measurements for theoretical comparison, it would be fruitful to calculate higher orders in $\frac{v_n\{2\}(p_\mathrm{T})}{v_n[2](p_\mathrm{T})}$ and r_n .

Appendix A

Coordinate System

The coordinate system used in this thesis is presented here.

A.1 Euclidean coordinates

This labels space points in conventional Euclidean coordinates, with the origin coinciding with the central point of the ALICE central barrel. Moreover, the z axis is taken to be the direction of travel of the beam. This is the convention used by high energy physics experiments at CERN. Figure A.1 shows the Euclidan coordinate system used in this work. The transverse $x - y$ plane is then the plane transverse to the beam direction, or the *transverse plane*. The transverse radius is then

$$r = \sqrt{x^2 + y^2} \ . \tag{A.1}$$

Transverse momentum, p_{T} , is then defined as the component of momentum in the transverse plane: $p_{\mathrm{T}}^2 = p_{\mathrm{x}}^2 + p_{\mathrm{y}}^2$. Particles interact near the origin at the *primary vertex*, whose z component in euclidean coordinates is denoted PV_z.

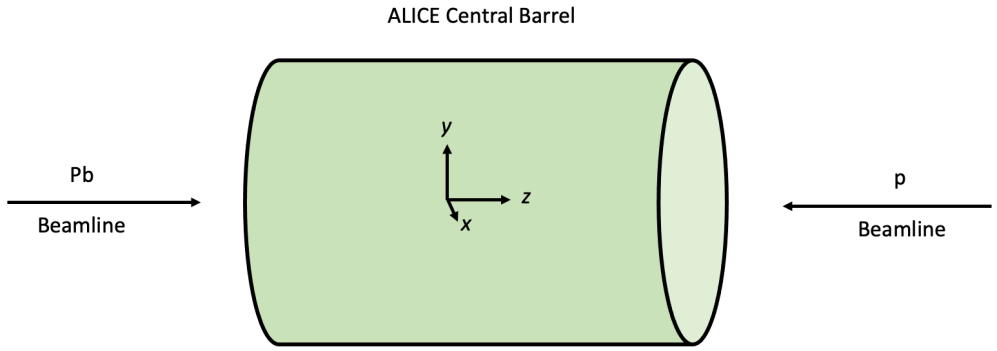

Figure A.1: Euclidian coordinates used throughout this thesis.

A.2 Detector Coordinates

The central barrel is radially symmetric, and it is common to use a form of spherical coordinates to describe the position of a detected particle. *azimuthal angle* is the angle a spatial point makes in the $x - y$ plane. To determine the the angle a particle makes in the $y - z$ plane, the concept known as *rapidity* is used.

Rapidity is a quantity that is invariant under a Lorentz boost and is defined as

$$y = \frac{1}{2} \ln \left(\frac{E + p_{\mathrm{L}}}{E + p_{\mathrm{L}}} \right), \tag{A.2}$$

where E is the relativistic energy $E = \sqrt{m^2 + p^2}$ in natural units, and p_{L} is the longitudinal momentum. In the limit where $m \ll p$, rapidity reduces to *psuedorapidity*, η. Psuedorapidity can be expressed as

$$\eta = -\ln \left[\tan \left(\frac{\theta}{2} \right) \right] , \tag{A.3}$$

where θ is the traditional polar angle. This is a reasonable approximation in high energy physics experiments when particles are travelling at momenta far greater than their rest mass. Figure A.2 shows the detector coordinate system superimposed on a cartoon of ALICE. When $\theta = 0°$, $\eta = 0$, and when $\theta = 90°$, $\eta = \infty$. As one approaches the beam axis from $\eta = 0$, increments of η become spatially closer together.

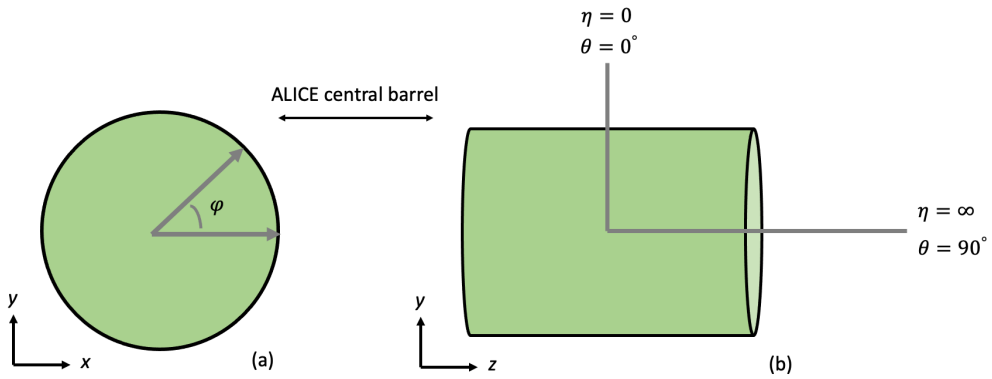

Figure A.2: **(a):** illustration of azimuthal angle, φ. **(b)**: illustration of psuedorapidity, η.

Appendix B

Systematics

This appendix shows for the ratio between the default and variational values in systematic checks. Also shown is the results for the Barlow test, which was used to determine if a systematic variation varied significantly from the default measurements.

B.1 Systematic variations in template fit and peripheral subtraction for $\frac{v_2\{2\}(p_T)}{v_2[2](p_T)}$

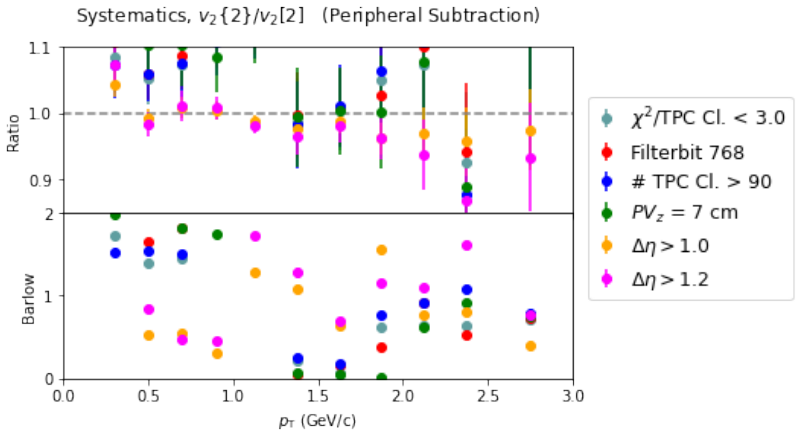

Figure B.1: The ratio between default and systematic values and the corresponding Barlow test for the observable $\frac{v_2\{2\}(p_T)}{v_2[2](p_T)}$ in p–Pb collisions at $\sqrt{s_{NN}} =$ 5.02 TeV **(peripheral subtraction method)**.

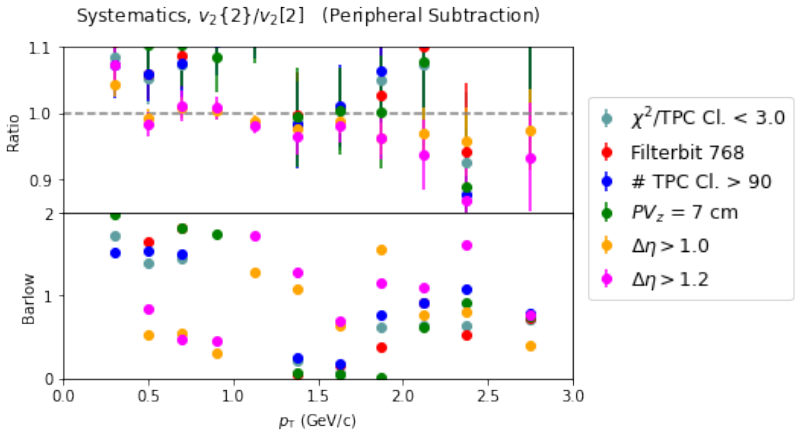

Figure B.2: The ratio between default and systematic values and the corresponding Barlow test for the observable $\frac{v_2\{2\}(p_T)}{v_2[2](p_T)}$ in p–Pb collisions at $\sqrt{s_{NN}} = 5.02$ TeV **(template fit method)**.

B.2 Systematic variations in template fit and peripheral subtraction for r_2

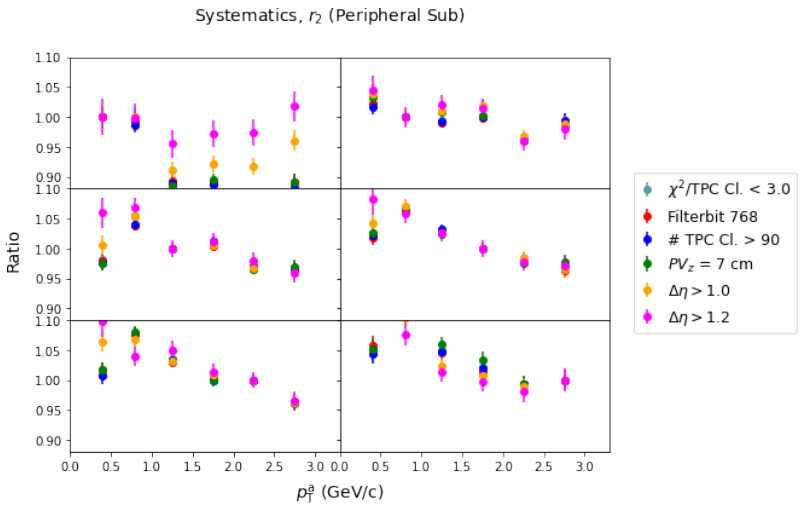

Figure B.3: The ratio between default and systematic values for the observable r_2 in p–Pb collisions at $\sqrt{s_{NN}} = 5.02$ TeV **(peripheral subtraction method)**.

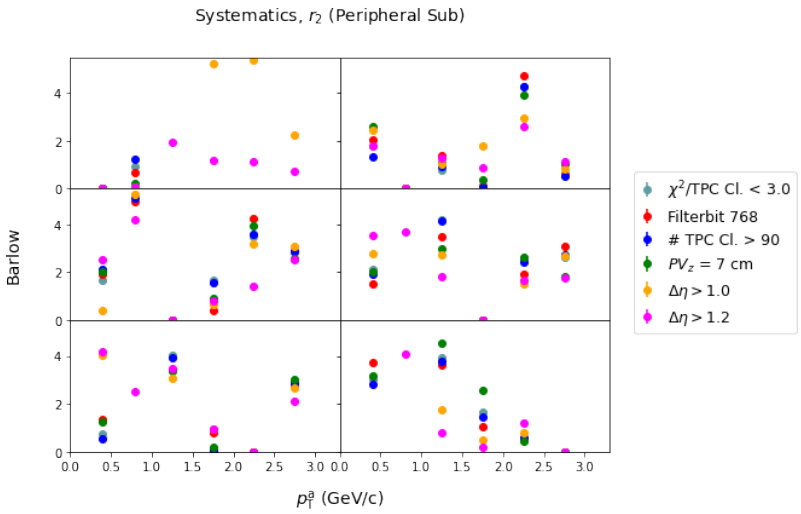

Figure B.4: The Barlow test for the observable r_2 in p–Pb collisions at $\sqrt{s_{\mathrm{NN}}}$ = 5.02 TeV **(peripheral subtraction method)**.

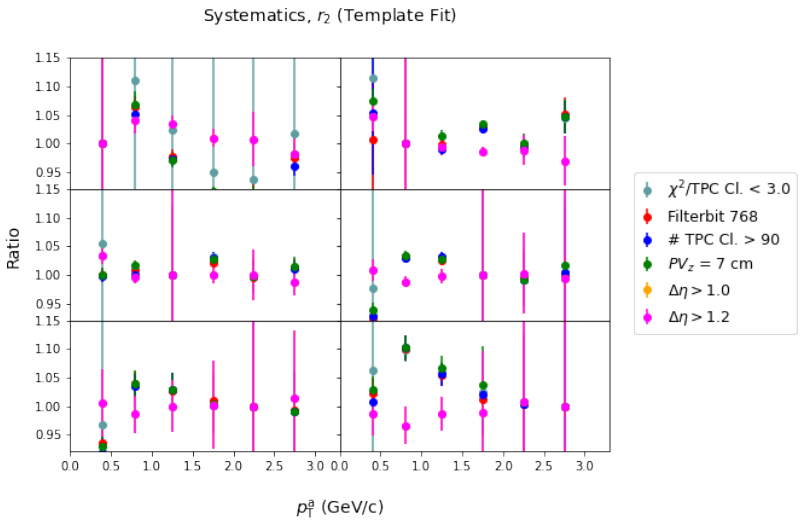

Figure B.5: The ratio between default and systematic values for the observable r_2 in p–Pb collisions at $\sqrt{s_{\mathrm{NN}}}$ = 5.02 TeV **(template fit method)**.

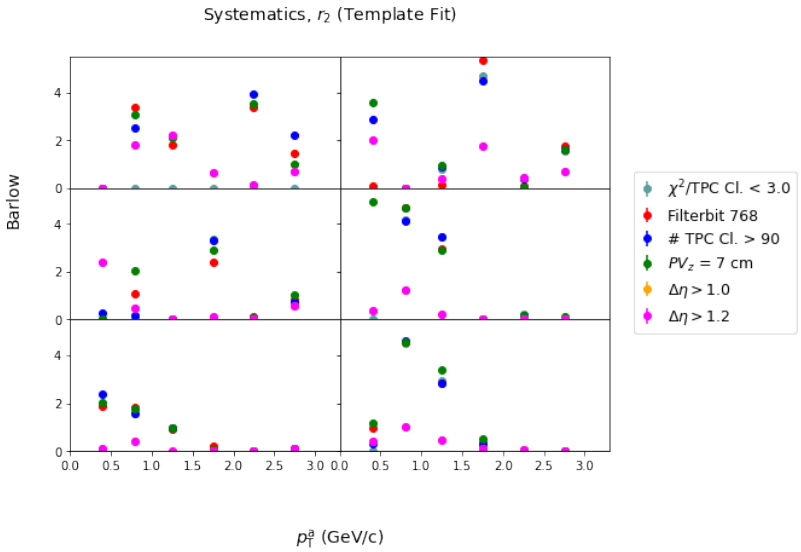

Figure B.6: The Barlow test for the observable r_2 in p–Pb collisions at $\sqrt{s_{\mathrm{NN}}}$ = 5.02 TeV **(template fit method)**.

Bibliography

[1] Peter W. Higgs. "Broken Symmetries and the Masses of Gauge Bosons". In: *Phys. Rev. Lett.* 13 (16 1964), pp. 508–509. DOI: 10.1103/PhysRevLett.13.508.

[2] F. Englert and R. Brout. "Broken Symmetry and the Mass of Gauge Vector Mesons". In: *Phys. Rev. Lett.* 13 (9 1964), pp. 321–323. DOI: 10.1103/PhysRevLett.13.321.

[3] G. S. Guralnik, C. R. Hagen, and T. W. B. Kibble. "Global Conservation Laws and Massless Particles". In: *Phys. Rev. Lett.* 13 (20 1964), pp. 585–587. DOI: 10.1103/PhysRevLett.13.585.

[4] Mark Thomson. "Modern particle physics". In: (2013).

[5] Marek Karliner and Jonathan L. Rosner. "Discovery of doubly-charmed Ξ_{cc} baryon implies a stable $(bb\bar{u}\bar{d})$ tetraquark". In: *Phys. Rev. Lett.* 119.20 (2017), p. 202001. DOI: 10.1103/PhysRevLett.119.202001.

[6] LHCb Collaboration. "Observation of $J/\psi p$ Resonances Consistent with Pentaquark States in $\Lambda_b^0 \to J/\psi K^- p$ Decays". In: *Phys. Rev. Lett.* 115 (7 2015), p. 072001. DOI: 10.1103/PhysRevLett.115.072001.

[7] Wikipedia. *File:Standard Model of Elementary Particles.svg — Wikipedia, The Free Encyclopedia", year = "2004"*. [Online; accessed 15-March-2022].

[8] David Griffiths. "Introduction to elementary particles". In: (2020).

[9] Francisco J Ynduráin. "The theory of quark and gluon interactions". In: (2007).

[10] Taizo Muta. "Foundations of quantum chromodynamics: an introduction to perturbative methods in gauge theories". In: (1998).

[11] Pok Man Lo et al. "Matching the Hagedorn mass spectrum with lattice QCD results". In: *Physical Review C* 92.5 (2015), p. 055206.

[12] Jerzy Bartke. "Introduction to relativistic heavy ion physics". In: (2008).

[13] A. Chaudhuri. "Viscous Hydrodynamic Model for Relativistic Heavy Ion Collisions". In: *Advances in High Energy Physics* 2013 (Jan. 2013). DOI: 10.1155/2013/693180.

[14] Peter Braun-Munzinger and Benjamin Dönigus. "Loosely-bound objects produced in nuclear collisions at the LHC". In: *Nuclear Physics A* 987 (2019), pp. 144–201. DOI: 10.1016/j.nuclphysa.2019.02.006.

[15] Edmond Iancu. "QCD in heavy ion collisions". In: *arXiv preprint:1205.0579* (2012).

[16] Tapan K. Nayak. "Probing the QCD phase structure using event-by-event fluctuations". In: *Journal of Physics: Conference Series* 1602.1 (2020), p. 012003. DOI: 10.1088/1742-6596/1602/1/012003.

[17] A. Bazavov et al. "Chiral crossover in QCD at zero and non-zero chemical potentials". In: *Physics Letters B* 795 (2019), pp. 15–21. ISSN: 0370-2693. DOI: doi.org/10.1016/j.physletb.2019.05.013.

[18] Rudolph C. Hwa and Xin-Nian Wang, eds. *Quark-gluon plasma 4*. Singapore: World Scientific, 2010. ISBN: 978-981-4293-28-0, 978-981-4465-88-5. DOI: 10.1142/7588.

[19] Raimond Snellings. "Elliptic flow: a brief review". In: *New Journal of Physics* 13.5 (2011), p. 055008. DOI: 10.1088/1367-2630/13/5/055008.

[20] S. Voloshin and Y. Zhang. "Flow study in relativistic nuclear collisions by Fourier expansion of azimuthal particle distributions". In: *Zeitschrift fr Physik C Particles and Fields* 70.4 (1996), pp. 665–671. DOI: 10.1007/s002880050141.

[21] ALICE Collaboration. "Higher Harmonic Anisotropic Flow Measurements of Charged Particles in Pb-Pb Collisions at $\sqrt{s_{NN}} = 2.76$ TeV". In: *Phys. Rev. Lett.* 107 (3 2011), p. 032301. DOI: 10.1103/PhysRevLett.107.032301.

[22] ALICE Collaboration. "Directed Flow of Charged Particles at Midrapidity Relative to the Spectator Plane in Pb-Pb Collisions at $\sqrt{s_{\rm NN}} = 2.76$ TeV". In: *Phys. Rev. Lett.* 111 (23 2013), p. 232302. DOI: 10.1103/PhysRevLett.111.232302.

[23] R.S. Bhalerao et al. "Relating Eccentricity Fluctuations to Density Fluctuations in Heavy-ion Collisions". In: *Acta Physica Polonica B* 50.6 (2019), p. 1165. DOI: 10.5506/aphyspolb.50.1165.

[24] R. J. Glauber. "Cross Sections in Deuterium at High Energies". In: *Phys. Rev.* 100 (1 1955), pp. 242–248. DOI: 10.1103/PhysRev.100.242.

[25] Gabriel Denicol, Akihiko Monnai, and Björn Schenke. "Moving Forward to Constrain the Shear Viscosity of QCD Matter". In: *Phys. Rev. Lett.* 116 (21 2016), p. 212301. DOI: 10.1103/PhysRevLett.116.212301.

[26] ALICE Collaboration. "Elliptic Flow of Charged Particles in Pb-Pb Collisions at $\sqrt{s_{NN}} = 2.76$TeV". In: *Phys. Rev. Lett.* 105 (25 2010), p. 252302. DOI: 10.1103/PhysRevLett.105.252302.

[27] ALICE Collaboration. "Searches for transverse momentum dependent flow vector fluctuations in Pb-Pb and p-Pb collisions at the LHC". In: *Journal of High Energy Physics* 2017.9 (2017). DOI: 10.1007/jhep09(2017)032.

[28] ALICE Collaboration. "Long-range angular correlations on the near and away side in p–Pb collisions at $\sqrt{s_{\mathrm{NN}}}$=5.02 TeV". In: *Physics Letters B* 719.1 (2013), pp. 29–41. ISSN: 0370-2693. DOI: https://doi.org/10.1016/j.physletb.2013.01.012.

[29] ATLAS Collaboration. "Observation of Associated Near-Side and Away-Side Long-Range Correlations in $\sqrt{s_{NN}}$=5.02 TeV Proton-Lead Collisions with the ATLAS Detector". In: *Phys. Rev. Lett.* 110 (18 2013), p. 182302. DOI: 10.1103/PhysRevLett.110.182302.

[30] CMS Collaboration. "Observation of long-range, near-side angular correlations in pPb collisions at the LHC". In: *Physics Letters B* 718.3 (2013), pp. 795–814. ISSN: 0370-2693. DOI: https://doi.org/10.1016/j.physletb.2012.11.025.

[31] ALICE Collaboration. "Investigations of Anisotropic Flow Using Multiparticle Azimuthal Correlations in *pp*, *p*−Pb, Xe-Xe, and Pb-Pb Collisions at the LHC". In: *Phys. Rev. Lett.* 123 (14 2019), p. 142301. DOI: 10.1103/PhysRevLett.123.142301.

[32] Shanshan Cao and Xin-Nian Wang. "Jet quenching and medium response in high-energy heavy-ion collisions: a review". In: *Reports on Progress in Physics* 84.2 (2021), p. 024301. DOI: 10.1088/1361-6633/abc22b.

[33] ALICE Collaboration. "Transverse momentum spectra and nuclear modification factors of charged particles in pp, p-Pb and Pb-Pb collisions at the LHC". In: *JHEP* 11 (2018), p. 013. DOI: 10.1007/JHEP11(2018)013. arXiv: 1802.09145 [nucl-ex].

[34] Nicolas Borghini, Phuong Mai Dinh, and Jean-Yves Ollitrault. "New method for measuring azimuthal distributions in nucleus-nucleus collisions". In: *Physical Review C* 63.5 (2001). DOI: 10.1103/physrevc.63.054906.

[35] Ulrich Heinz, Zhi Qiu, and Chun Shen. "Fluctuating flow angles and anisotropic flow measurements". In: *Phys. Rev. C* 87 (3 2013), p. 034913. DOI: 10.1103/PhysRevC.87.034913.

[36] Fernando G. Gardim et al. "Breaking of factorization of two-particle correlations in hydrodynamics". In: *Physical Review C* 87.3 (2013). DOI: 10.1103/physrevc.87.031901.

[37] B. Alver and G. Roland. "Collision-geometry fluctuations and triangular flow in heavy-ion collisions". In: *Phys. Rev. C* 81 (5 2010), p. 054905. DOI: 10.1103/PhysRevC.81.054905.

[38] B. Alver et al. "System Size, Energy, Pseudorapidity, and Centrality Dependence of Elliptic Flow". In: *Physical Review Letters* 98.24 (2007). DOI: 10.1103/physrevlett.98.242302.

[39] Igor Kozlov et al. "Transverse momentum structure of pair correlations as a signature of collective behavior in small collision systems". In: *arXiv* (2014). DOI: 10.48550/ARXIV.1405.3976.

[40] S. Roesler, R. Engel, and J. Ranft. "The Monte Carlo Event Generator DPMJET-III". In: Springer Berlin Heidelberg, 2001, pp. 1033–1038. DOI: 10.1007/978-3-642-18211-2_166.

[41] ALICE Collaboration. "Harmonic decomposition of two particle angular correlations in Pb–Pb collisions at $\sqrt{s_{\mathrm{NN}}}$=2.76 TeV". In: *Physics Letters B* 708.3 (2012), pp. 249–264. ISSN: 0370-2693. DOI: https://doi.org/10.1016/j.physletb.2012.01.060.

[42] ATLAS Collaboration. "Measurement of elliptic and higher order flow from ATLAS experiment at the LHC". In: *Journal of Physics G: Nuclear and Particle Physics* 38.12 (2011), p. 124012. DOI: 10.1088/0954-3899/38/12/124012.

[43] ALICE Collaboration. "Triggered di-hadron correlations in Pb–Pb collisions from the ALICE experiment". In: *Journal of Physics G: Nuclear and Particle Physics* 38.12 (2011), p. 124091. DOI: 10.1088/0954-3899/38/12/124091.

[44] ATLAS Collaboration. "Measurement of the centrality dependence of the charged-particle pseudorapidity distribution in lead–lead collisions at $\sqrt{s_{\mathrm{NN}}} = 2.76$ TeV with the ATLAS detector". In: *Physics Letters B* 710.3 (2012), pp. 363–382. DOI: 10.1016/j.physletb.2012.02.045.

[45] Nicolas Borghini, Phuong Mai Dinh, and Jean-Yves Ollitrault. "Is the analysis of flow at the CERN Super Proton Synchrotron reliable?" In: *Phys. Rev. C* 62 (3 2000), p. 034902. DOI: 10.1103/PhysRevC.62.034902.

[46] CMS Collaboration. "Observation of long-range, near-side angular correlations in proton-proton collisions at the LHC". In: *Journal of High Energy Physics* 2010.9 (2010). DOI: 10.1007/jhep09(2010)091.

[47] PHOBOS Collaboration. "High transverse momentum triggered correlations over a large pseudorapidity acceptance in Au+Au collisions at $\sqrt{s_{\mathrm{NN}}}$ = 200 GeV". In: *Physical Review Letters* 104.6 (2010). DOI: 10.1103/physrevlett.104.062301.

[48] Alice Ohlson. "Collective behavior in small systems". In: *Nuclear Physics A* 967 (2017), pp. 97–104.

[49] K. Werner, Iu. Karpenko, and T. Pierog. ""Ridge" in Proton-Proton Scattering at 7 TeV". In: *Physical Review Letters* 106.12 (2011). DOI: 10.1103/physrevlett.106.122004.

[50] M G Ryskin, A D Martin, and V A Khoze. "Probes of multiparticle production at the LHC". In: *Journal of Physics G: Nuclear and Particle Physics* 38.8 (2011), p. 085006. DOI: 10.1088/0954-3899/38/8/085006.

[51] Cheuk-Yin Wong. "Momentum-kick model description of the ridge in $\Delta\phi - \Delta\eta$ correlations in pp collisions at 7 TeV". In: *Physical Review C* 84.2 (2011). DOI: 10.1103/physrevc.84.024901.

[52] Kevin Dusling and Raju Venugopalan. "Comparison of the color glass condensate to dihadron correlations in proton-proton and proton-nucleus collisions". In: *Physical Review D* 87.9 (2013). DOI: 10.1103/physrevd.87.094034.

[53] E Avsar et al. "Eccentricity and elliptic flow inipp/icollisions at the LHC". In: *Journal of Physics G: Nuclear and Particle Physics* 38.12 (2011), p. 124053. DOI: 10.1088/0954-3899/38/12/124053.

[54] Wei-Tian Deng, Zhe Xu, and Carsten Greiner. "Elliptic and triangular flow and their correlation in ultrarelativistic high multiplicity proton–proton collisions at 14 TeV". In: *Physics Letters B* 711.3-4 (2012), pp. 301–306. DOI: 10.1016/j.physletb.2012.04.010.

[55] Piotr Boż ek. "Flow and interferometry in (3 1)-dimensional viscous hydrodynamics". In: *Physical Review C* 85.3 (2012). DOI: 10.1103/physrevc.85.034901.

[56] M. Strikman. "Transverse nucleon structure and multiparton interactions". In: *Acta Physica Polonica B* 42.12 (2011), p. 2607. DOI: 10.5506/aphyspolb.42.2607.

[57] Piotr Bożek and Wojciech Broniowski. "Correlations from hydrodynamic flow in pPb collisions". In: *Physics Letters B* 718.4 (2013), pp. 1557–1561. ISSN: 0370-2693. DOI: https://doi.org/10.1016/j.physletb.2012.12.051.

[58] Kevin Dusling and Raju Venugopalan. "Explanation of systematics of CMS p+Pb high multiplicity di-hadron data at $\sqrt{s_{\rm NN}}$=5.02 TeV". In: *Physical Review D* 87.5 (2013). DOI: 10.1103/physrevd.87.054014.

[59] Yuri V. Kovchegov and Douglas E. Wertepny. "Long-range rapidity correlations in heavy–light ion collisions". In: *Nuclear Physics A* 906 (2013), pp. 50–83. DOI: 10.1016/j.nuclphysa.2013.03.006.

[60] Adam Bzdak et al. "Initial-state geometry and the role of hydrodynamics in proton-proton, proton-nucleus, and deuteron-nucleus collisions". In: *Physical Review C* 87.6 (2013). DOI: 10.1103/physrevc.87.064906.

[61] Li Yan and Jean-Yves Ollitrault. "Universal Fluctuation-Driven Eccentricities in Proton-Proton, Proton-Nucleus, and Nucleus-Nucleus Collisions". In: *Physical Review Letters* 112.8 (2014). DOI: 10.1103/physrevlett.112.082301.

[62] Guo-Liang Ma and Adam Bzdak. "Long-range azimuthal correlations in proton–proton and proton–nucleus collisions from the incoherent scattering of partons". In: *Physics Letters B* 739 (2014), pp. 209–213. DOI: 10.1016/j.physletb.2014.10.066.

[63] Björn Schenke and Raju Venugopalan. "Eccentric protons? Sensitivity of flow to system size and shape in p+p, p+Pb and Pb+Pb collisions". In: *Physical Review Letters* 113.10 (2014). DOI: 10.1103/physrevlett.113.102301.

[64] Paul M. Chesler. "Colliding Shock Waves and Hydrodynamics in Small Systems". In: *Physical Review Letters* 115.24 (2015). DOI: 10.1103/physrevlett.115.241602.

[65] Lyndon Evans and Philip Bryant. "LHC Machine". In: *Journal of Instrumentation* 3.08 (2008), S08001–S08001. DOI: 10.1088/1748-0221/3/08/s08001.

[66] D. Boussard et al. "The LHC superconducting cavities". In: vol. 2. Feb. 1999, 946 –948 vol.2. ISBN: 0-7803-5573-3. DOI: 10.1109/PAC.1999.795409.

[67] The ALICE Collaboration. "The ALICE experiment at the CERN LHC". In: *Journal of Instrumentation* 3.08 (2008), S08002–S08002. DOI: 10.1088/1748-0221/3/08/s08002.

[68] I. Antcheva et al. "ROOT — A C framework for petabyte data storage, statistical analysis and visualization". In: *Computer Physics Communications* 180.12 (2009), pp. 2499–2512. DOI: 10.1016/j.cpc.2009.08.005.

[69] R. Brun et al. "Computing in ALICE". In: *Nuclear Instruments and Methods in Physics Research Section A: Accelerators, Spectrometers, Detectors and Associated Equipment* 502.2 (2003). Proceedings of the VIII International Workshop on Advanced Computing and Analysis Techniques in Physics Research, pp. 339–346. ISSN: 0168-9002. DOI: https://doi.org/10.1016/S0168-9002(03)00440-6.

[70] B. Efron. "Bootstrap Methods: Another Look at the Jackknife". In: *The Annals of Statistics* 7.1 (1979), pp. 1 –26. DOI: 10.1214/aos/1176344552.

[71] Roger Barlow. *Systematic Errors: facts and fictions*. 2002. DOI: 10.48550/ARXIV.HEP-EX/0207026.

[72] CMS Collaboration. "Studies of azimuthal dihadron correlations in ultra-central PbPb collisions at $\sqrt{s_{\mathrm{NN}}}$ =2.76 TeV". In: *Journal of High Energy Physics* 2014.2 (2014). DOI: 10.1007/jhep02(2014)088.

[73] S. Agostinelli et al. "Geant4—a simulation toolkit". In: *Nuclear Instruments and Methods in Physics Research Section A: Accelerators, Spectrometers, Detectors and Associated Equipment* 506.3 (2003), pp. 250–303. ISSN: 0168-9002. DOI: https://doi.org/10.1016/S0168-9002(03)01368-8.

[74] ATLAS Collaboration. "Observation of Long-Range Elliptic Azimuthal Anisotropies in $\sqrt{s}$ = 13 and 2.76 TeV *pp* Collisions with the ATLAS Detector". In: *Phys. Rev. Lett.* 116 (17 2016), p. 172301. DOI: 10.1103/PhysRevLett.116.172301.

[75] M. Aaboud et al. "Correlated long-range mixed-harmonic fluctuations measured in pp, p+Pb and low-multiplicity Pb+Pb collisions with the ATLAS detector". In: *Physics Letters B* 789 (2019), pp. 444–471. ISSN: 0370-2693. DOI: https://doi.org/10.1016/j.physletb.2018.11.065.

[76] You Zhou. "Anisotropic flow measurements in Pb–Pb collisions at = 5.02 TeV with ALICE". In: *Journal of Physics: Conference Series* 779 (2017), p. 012055. DOI: 10.1088/1742-6596/779/1/012055.

[77] ALICE Collaboration. "Energy dependence and fluctuations of anisotropic flow in Pb-Pb collisions at $\sqrt{s_{\mathrm{NN}}}$=5.02 and 2.76 TeV". In: *Journal of High Energy Physics* 2018.7 (2018). DOI: 10.1007/jhep07(2018)103.

[78] Piotr Bozek and Rupam Samanta. "Factorization breaking for higher moments of harmonic flow". In: *Phys. Rev. C* 105.3 (2022), p. 034904. DOI: 10.1103/PhysRevC.105.034904. arXiv: 2109.07781 [nucl-th].

[79] CMS Collaboration. "Evidence for transverse-momentum- and pseudorapidity-dependent event-plane fluctuations in PbPb and *p*Pb collisions". In: *Phys. Rev. C* 92 (3 2015), p. 034911. DOI: 10.1103/PhysRevC.92.034911.

[80] Igor Kozlov et al. *Transverse momentum structure of pair correlations as a signature of collective behavior in small collision systems*. 2014. DOI: 10.48550/ARXIV.1405.3976.